JAMES | Journal of Advances in Modeling Earth Systems

RESEARCH ARTICLE
10.1029/2025MS005428

Can Eulerian Eddy Diffusivity Be Inferred From Lagrangian Trajectories?

Yueyang Lu[1,2], **Igor Kamenkovich**[1], **and Pavel Berloff**[3]

[1]Rosenstiel School of Marine, Atmospheric, and Earth Science, University of Miami, Miami, FL, USA, [2]Center for Ocean-Atmospheric Prediction Studies, Florida State University, Tallahassee, FL, USA, [3]Department of Mathematics, Imperial College London, London, UK

Key Points:

- A new approach to calculating Eulerian mesoscale eddy diffusivity from Lagrangian particle trajectories is proposed
- The estimated eddy diffusivity is close to the Eulerian counterpart when the particle resolution is higher than one deformation radius
- The study highlights the potential of Lagrangian measurements to provide insights into local eddy mixing processes in the ocean

Correspondence to:

I. Kamenkovich and Y. Lu,
ikamenkovich@miami.edu;
yl24q@fsu.edu

Citation:

Lu, Y., Kamenkovich, I., & Berloff, P. (2026). Can Eulerian eddy diffusivity be inferred from Lagrangian trajectories? *Journal of Advances in Modeling Earth Systems*, *18*, e2025MS005428. https://doi.org/10.1029/2025MS005428

Received 15 AUG 2025
Accepted 6 APR 2026

Abstract Lagrangian particle trajectories are widely used to characterize tracer dispersion and mixing driven by mesoscale currents ("eddies"), leading to estimates of eddy diffusivity that can in turn be used in non-eddy-resolving and eddy-permitting ocean models. These Lagrangian estimates, however, are asymptotic quantities and cannot capture spatial and temporal variability in the eddy-driven mixing. This study explores the use of Lagrangian particles to calculate the local ("Eulerian") characteristics of tracer distribution and evolution in eddying flows, including tracer concentrations, eddy-driven tracer fluxes and diffusivities. The proposed "hybrid" Eulerian-Lagrangian approach assumes that continuous tracer evolutions can be described by motions of a finite number of fluid particles (parcels). Multiple tracer realizations can then be readily generated from a single realization of Lagrangian trajectories. Using an idealized eddy-resolving double-gyre ocean model, we found that these hybrid estimates closely match the direct, tracer-based estimates, as long as the density of spatial particle coverage is sufficiently high. Specifically, the estimates are reliable until the particles' resolution decreases to about one particle per the first deformation radius. The proposed approach to estimating Eulerian eddy transport properties from Lagrangian particle trajectories may serve as a strong motivation for conducting Lagrangian field experiments with large particle ensembles.

Plain Language Summary Eddy diffusivity describes the strength of mixing driven by the ocean's swirling motions (eddies) and is defined locally because the eddy mixing varies from place to place. Lagrangian observations, such as drifters and floats that drift with ocean currents, track the movement of water and are commonly used to estimate eddy mixing through long-time statistical averages (asymptotically). However, these estimates represent eddy mixing averaged over large spatial and temporal scales and may blend variations at local spaces and times. This study uses Lagrangian particles—an idealized representation of drifters and floats in numerical ocean models—to directly estimate Eulerian eddy diffusivity. The proposed approach is computationally efficient and accurately reproduces local diffusivity with as few as one particle per eddy length scale. These results highlight the potential of Lagrangian measurements to provide detailed insights into local eddy mixing processes in the ocean.

1. Introduction

Mesoscale eddies, defined here as currents on spatial scales between 20 and 200 km, play a key role in distribution of various oceanic properties ("tracers"). To the leading order, the eddy-driven stirring of water is assumed to lead to mixing and homogenization of dissolved tracers along isopycnal surfaces (Abernathey et al., 2022; Vallis, 2017). The efficiency of the mixing can be defined as the ability of mesoscale eddies to induce a tracer flux in the presence of background large-scale tracer gradient. The calculation of the flux from the large-scale properties is useful for both the interpretation of observational data and climate predictions, as most global ocean models used for this purpose cannot resolve the oceanic mesoscale and the eddy-induced flux must be parameterized. The most commonly used method is based on a linear relationship between the large-scale, eddy-driven tracer flux $\mathbf{F_e}$ and the large-scale tracer gradient $\nabla_{\mathbf{L}} c$:

$$\mathbf{F_e} = -\mathbf{K}\nabla_{\mathbf{L}} c \tag{1}$$

where $\mathbf{K}$ is a transport tensor, whose symmetric component is a diffusivity tensor that quantifies the properties of eddy mixing. This flux-gradient relation is based on an analogy between the eddy-induced mixing and molecular diffusion (Taylor, 1921), and is further motivated by the mixing length theory (Prandtl, 1925; Vallis, 2017). The

utility of the eddy diffusivity tensor has motivated numerous efforts to estimate it in the real ocean and numerical simulations. There are three main approaches, as reviewed by Qian et al. (2019): (a) the local Eulerian method, based on continuous tracer variances or tracer gradients (e.g., Osborn & Cox, 1972; Plumb & Mahlman, 1987), (b) the nonlocal (asymptotic) Lagrangian method, based on tracer clouds or particle trajectories (Garrett, 1983; Griesel et al., 2010), and (c) the approaches based on estimating an "effective diffusivity" from the geometry of instantaneous tracer contours (Marshall et al., 2006; Nakamura, 1996). The effective diffusivity is defined on the contour-based coordinate instead of the geographic coordinate. So, it is not strictly local and it is not easy to link effective diffusivity to the Eulerian local mixing rate in along-contour direction (Marshall et al., 2006).

The Eulerian eddy diffusivity computed from the flux-gradient relationship (Equation 1) is most directly relevant to the parameterization of isopycnal eddy-induced mixing (Griffies, 1998). Note here we are concerned with along isopycnal mixing of tracers, and do not address eddy-induced mass fluxes that play an important but distinct role in distribution of tracers (Gent et al., 1995; Gent & McWilliams, 1990). Generally speaking, if the transport tensor is known exactly at each location, the eddy fluxes would be accurately reproduced from the large-scale gradient. However, the downside of this approach is the need for detailed knowledge of multiple tracer fields at high spatial resolution and concurrent eddy fluxes. For example, while at least two tracers are needed to estimate the four components of the lateral transport tensor, it is preferred to use a larger number of tracers for more stable estimates given the sensitivity of the tensor values to tracer distribution (Bachman et al., 2015; Bachman & Fox-Kemper, 2013). It should be emphasized that none of these estimates yield a perfect transport tensor—namely, a unique tensor capable of accurately reproducing the eddy fluxes of every tracer, assuming such a quantity exists (Haigh et al., 2020; Kamenkovich et al., 2021; Lu et al., 2022; Sun et al., 2021). These difficulties in estimating diffusivity may indicate fundamental limitations in the validity of Eulerian diffusivity as a model of eddy tracer dynamics. Additionally, although this approach can be used in eddy-resolving numerical simulations (e.g., Abernathey et al., 2013; Bachman et al., 2020; T. Uchida et al., 2023; Zhang & Wolfe, 2022), it would be extremely challenging in the real ocean since releasing and tracking multiple tracers is not feasible.

Lagrangian observations are becoming increasingly abundant, from surface drifters (Lumpkin et al., 2017; Mariano et al., 2016) to subsurface floats (Lebedev et al., 2007) that follow ocean currents at different depths over a long period of time. Many valuable insights into ocean pathways and dynamics have been inferred from Lagrangian data (see reviews by J. LaCasce (2008); Sebille et al. (2018); Prants (2025)). As stated earlier, the Lagrangian eddy diffusivity can be estimated from drifters (Zhurbas et al., 2014; Zhurbas & Oh, 2003, 2004), floats (LaCasce et al., 2014; Lumpkin et al., 2002), as well as numerically simulated particles that represent those observations in the model (Griesel et al., 2010; Zhang & Wolfe, 2024). The Lagrangian diffusivity is computed from ensembles of drifters or particles using displacement variance (dispersion) or velocity autocorrelation (Davis, 1991; Rypina et al., 2012), or from particle pairs using their separation rates (Poje et al., 2014). Similarly powerful tracer-based Lagrangian methods utilize tracer cloud dispersion and contour evolution, as demonstrated in real-ocean tracer release experiments such as the North Atlantic Tracer Release Experiment (Ledwell et al., 1998) and the Diapycnal and Isopycnal Mixing Experiment in the Southern Ocean (Gille et al., 2007), as well as numerical simulations (Abernathey & Marshall, 2013). All these Lagrangian methods rely on asymptotic statistics of particle and tracer concentration over length- and time-scales that are much longer than the local correlation scales (e.g., scale of mesoscale eddies). The Lagrangian diffusivities are, therefore, inherently nonlocal in both time and space, a key property that differs from the Eulerian eddy diffusivity quantifying the local mixing. A number of previous studies have attempted to estimate diffusivities from Lagrangian data (e.g., Rühs et al., 2018; Zhurbas & Oh, 2003) by employing the formulation proposed by Davis (1991). The Davis diffusivity—computed from the autocorrelation between residual (full minus Eulerian mean) velocities and displacements of particles originating from certain locations—is not a pure Eulerian since it replies on asymptotic statistics (J. LaCasce, 2008; Rühs et al., 2018). Though in theory the Davis diffusivity should approach the Eulerian diffusivity (Equation 1) when the time lag for autocorrelation is greater than the time scales of target eddies, previous studies have shown that the two estimates are generally different (Griesel et al., 2014).

Rigorously speaking, the Eulerian and Lagrangian eddy diffusivities are equivalent only in the idealized, homogeneous and stationary turbulence in the absence of large-scale flows. In reality, the eddy transport is spatially inhomogeneous, non-stationary, anisotropic and is strongly modulated by the large-scale advection (Ferrari & Nikurashin, 2010). Direct comparisons of Eulerian and Lagrangian diffusivities in idealized (Abernathey et al., 2013) and realistic simulations (Griesel et al., 2014) reveal their differences, which can be larger in more complex flows. Most importantly, Lagrangian estimates may underestimate spatial variations and anisotropy in

diffusivity, due to the nonlocal nature of the method (Bachman et al., 2020; Griesel et al., 2010; Kamenkovich et al., 2021; Rypina et al., 2012). The significance of such complexity for global tracer distributions has yet to be demonstrated and smoother, large-scale Lagrangian estimates can prove to be more practical for applications in non-eddy-resolving numerical models. At the same time, important features in tracer fields, such as tracer fronts within the Gulf Stream extension, can be highly sensitive to local variations in diffusivity (Lu & Kamenkovich, 2025). Careful application of novel Lagrangian methods would be necessary to obtain accurate diffusivity estimates in these situations.

Given the importance of the Eulerian diffusivity in eddy parameterizations and the rich information provided by Lagrangian measurements (particles), this study explores the potential of using Lagrangian particles to directly calculate the Eulerian eddy diffusivity. We will map Lagrangian trajectories onto instantaneous Eulerian fields, from which arbitrary tracer concentrations can be derived. The key idea behind it is that particles can represent fluid parcels that carry water volume and tracer content, as proposed earlier by Bennett (2006) and J. LaCasce (2008) (also see a review by Haine et al. (2025)). Wagner et al. (2019) recently validated this idea by showing that the tracer spreading reconstructed from Lagrangian particles is consistent with the Eulerian field derived from the advective-diffusive equations in an ocean general circulation model. Furthermore, Jiang and Haine (2025b) built a tracer budget following individual Lagrangian particle trajectories, and used it to analyze the evolution of Subpolar North Atlantic salinity anomalies (Jiang & Haine, 2025a).

This study uses Lagrangian particle trajectories to simulate continuous distributions of idealized color-dye tracers. These tracer distributions, together with the particle velocities, are then used to derive the eddy tracer fluxes and infer the Eulerian diffusivity from the flux–gradient relation. To our knowledge, the idea of estimating the Eulerian diffusivity solely from Lagrangian particle trajectories has not been attempted before. Our novel hybrid Lagrangian-Eulerian approach is both computationally efficient—since particle trajectories only need to be simulated once to generate multiple tracer realizations—and numerically accurate, as it avoids the spurious numerical diffusion common in finite-element and finite-difference methods. Note that the eddy advection tensor, which is another important part of the eddy transport (Haigh et al., 2020), is not discussed here.

The rest of the paper is organized as follows. Section 2 introduces the ocean model and describes the methods used to simulate Lagrangian particles and to calculate the hybrid estimates. The results of the new hybrid method are discussed and compared with the conventional continuous method in Section 3, with conclusions presented in Section 4.

2. Model and Methods

2.1. Primitive Equation Ocean Model

This study uses a high-resolution wind-driven, adiabatic, shallow water model in an idealized domain, based on the Modular Ocean Model version 6 (MOM6; Adcroft, 2019). The model represents the mid-latitude, double-gyre ocean circulation in the Northern Hemisphere and was used in Lu and Kamenkovich (2025). The computational domain has the same length and width of $L_x = L_y = 3{,}840$ km, solid lateral walls and a flat bottom. The model has a free surface and three isopycnal layers. It is driven by an idealized steady, asymmetric, and tilted wind stress τ, and dissipated by bottom stress and viscous stress. The wind stress is expressed as (Berloff, 2015):

$$\tau_x = \frac{\tau_0}{2}\left[1 + \cos\left(\frac{2\pi(mx - y + L_y/2)}{(1+m)L_y}\right)\right], \tag{2a}$$

$$\tau_y = m\tau_x, \tag{2b}$$

The bottom stress is represented by a linear drag law that depends on a prescribed near-bottom flow speed $|\mathbf{u}_*|$ and coefficient C_d. The viscous stress tensor is parameterized by Laplacian viscosity ν. No normal flux and free slip boundary conditions at lateral walls are used. The key parameters are summarized in Table 1, and additional details can be found in Lu and Kamenkovich (2025).

The horizontal resolution is 3.75 km, sufficient to resolve the second deformation radius Rd_2, which is approximately 14 km in the middle of the domain. The model is spun up from the state of rest and driven by steady

Table 1
List of Parameters for the High-Resolution Model

Parameter	Value	Description
$L_x \times L_y$	3,840 × 3,840 km	Horizontal domain dimensions
Δx	3.75 km	Horizontal fine grid spacing
H_1, H_2, H_3	(0.3, 0.7, 3) km	Initial isopycnal layer thicknesses
f_0	4.4×10^{-5} s^{-1}	Coriolis parameter at the southern boundary
β	2×10^{-11} m^{-1} s^{-1}	Meridional gradient of Coriolis parameter
ρ_0	1035 kg m^{-3}	Reference density
ν	100 m^2 s^{-1}	Horizontal Laplacian viscosity
g	9.8 m s^{-2}	Gravity
g'	(0.01, 0.003) m s^{-2}	Reduced gravities at the upper interface of layer $k = 2, 3$
Rd_1, Rd_2	(23.6, 13.6) km	First and second Rossby deformation radii at mid-basin
τ_0	0.22 N m^{-2}	Wind stress amplitude
C_d	0.003	Linear bottom drag coefficient
$\lvert \mathbf{u}_* \rvert$	0.1 m s^{-1}	Near-bottom velocity magnitude
κ_{tr}	100 m^2 s^{-1}	Background isopycnal tracer diffusivity

Note. Note that the deformation radii are smaller than those reported in Lu and Kamenkovich (2025) because they are at the middle latitude while Lu and Kamenkovich (2025) reported the radii at the southernmost latitude.

wind forcing for 20 years to reach a statistically steady flow. The simulated flow consists of a well-developed analog of the Gulf Stream and a vigorous mesoscale eddy field (Figure 1a).

For a rough estimate of the shortest length scale still represented at this spatial resolution, we calculate the zonal wavenumber spectrum of eddy kinetic energy (EKE) (Figure 1b). The spectral slope follows the −5 power for the length scales shorter than approximately 800 km, but then further steepens starting at around Rd_2 and sharply falls off for scales shorter than 11.25 km—3 times the grid spacing. We conclude that the shortest length scale

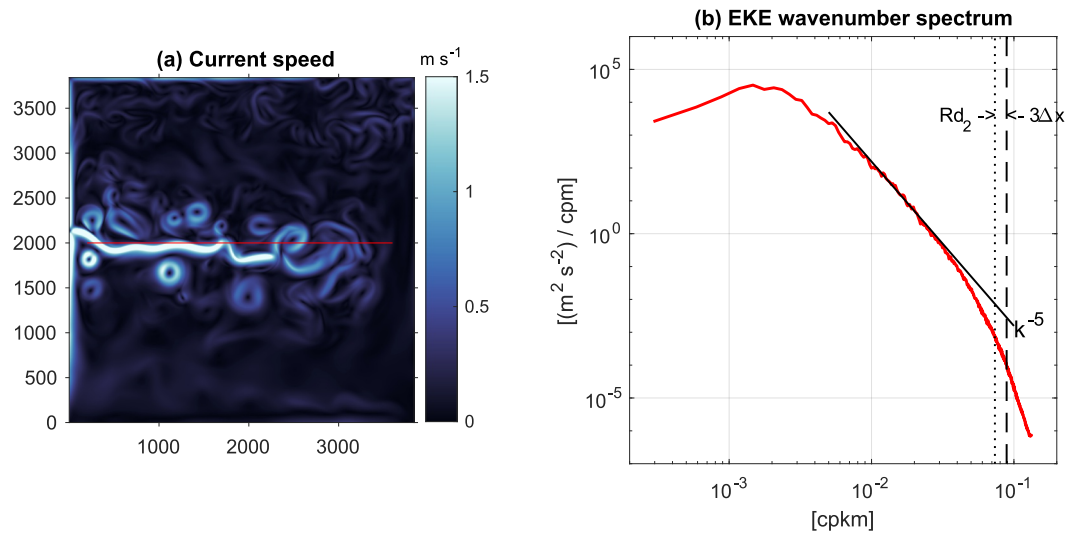

Figure 1. (a) Current speed in the upper layer at day 120 years 2. (b) The 2-year averaged zonal (one-dimensional) spectrum of EKE at the latitude of 2,000 km in the upper layer. The spectrum is computed from the meridional eddy velocity fields, defined as deviations from the 2-year averaged meridional velocity. The data within 200 km from the eastern and western boundaries are excluded before computing the spectra (see the red line in (a)). A spatial linear trend is subtracted and a Hann window is then applied. The second deformation radius Rd_2 (13.6 km) is shown as the dotted vertical line, the grid spacing timed by a factor of 3 (11.25 km) is shown as the dashed vertical line, and a −5 spectral slope is shown in solid black.

dynamically resolved in this simulation is approximately $3 * \Delta x = 11.25$ km. The model is, therefore, mesoscale resolving.

After the initial spin-up of 20 years, fixed-buoyancy particles are released in the top model layer at the beginning of year 21 and are simulated for 2 years. The particles are advected offline by the two-dimensional, 6-hourly-averaged model velocity field. For calculating the Eulerian eddy diffusivity, we also simulated eight idealized passive tracers initialized from the beginning of year 21 over the same 2 years. The initial tracer distributions (Appendix A) were linearly independent and remained so throughout the simulations, since the tracer equation is linear with respect to tracer concentration. We did not use relaxation for tracers, both because we focus on transient solutions during the 2 years, and because we wanted to avoid the dependence of diffusivity on the relaxation time scale (Haigh & Berloff, 2021).

2.2. Lagrangian Particle Trajectories

The position $\mathbf{X}$ of a virtual Lagrangian particle at time $t + \Delta t$ is calculated by:

$$\mathbf{X}(t + \Delta t) = \mathbf{X}(t) + \int_t^{t+\Delta t} \mathbf{u}(\mathbf{X}(\tau), \tau)\, \mathrm{d}\tau, \tag{3}$$

where Δt is the time step, and $\mathbf{u}(\mathbf{X}, t)$ is the Lagrangian velocity $\mathrm{d}\mathbf{X}(t)/\mathrm{d}t$ calculated as the Eulerian velocity at $\mathbf{X}(t)$. We use an adaptive fourth order Runge–Kutta method ("RK45") to integrate Equation 3 and bi-linear interpolation in space and time to estimate the velocity at the position and time of the particle (Rypina et al., 2012). We also tried cubic interpolation in space for the velocity but it did not noticeably affect the results of our study.

We release 1 048 576 $\left(1024^2\right)$ particles in 6 consecutive 130-day segments with the first 10 days of each segment overlapped by the 10 last days of the previous segment, providing a 2-year Lagrangian simulation in total. The particles are initially uniformly distributed across the domain in the upper layer, with one particle in each grid cell, leading to the "Lagrangian" spatial resolution of 1 particle per 3.75 km. We also released another set of particles (with the same number) with different initial distributions (shifting eastward by 1.875 km) and the results remain nearly identical. Thus, we argue that the initial particle distributions are not important for the main conclusions of this study. The particles do not leave the upper layer, with the exception of the small number of particles that cross the solid lateral boundaries due to numerical errors and are subsequently discarded.

2.3. Eulerian Eddy Diffusivity Tensor

The Eulerian diffusivity for a layered model is calculated by inversion of the flux-gradient relation Equation 1 (Bachman et al., 2020; Lu et al., 2022):

$$\mathbf{K}^E \coloneqq K_{ij}^E = -F_{i\beta}\left[\langle \overline{h} \rangle \partial_j \langle \overline{c}_\beta \rangle\right]^\dagger, \tag{4}$$

where i and j are used to index the horizontal coordinates, summation over repeated indices is assumed, β is used to indicate each of the different tracers, h is layer thickness. $\mathbf{K}^E$ is a 2×2 eddy transport tensor. The eddy tracer flux, $F_{i\beta}\left(\coloneqq \mathbf{F}_e^E\right)$, is defined as the difference between the full tracer flux and the flux due to the large-scale advection (omitting the tracer index β hereafter)

$$\mathbf{F}_e^E = \langle \overline{\mathbf{u}hc} \rangle - \langle \overline{\mathbf{u}h} \rangle \langle \overline{c} \rangle. \tag{5}$$

This form of eddy flux quantifies all the advective eddy contributions to the large-scale tracer in isopycnal formulation, which is arguably the most complete way to define the eddy effects in isopycnal coordinates (Sun et al., 2025; Uchida, Deremble, & Popinet, 2022; Uchida, Jamet, et al., 2022; Young, 2012). As stated earlier, we focus on the eddy mixing along isopycnals and exclude the eddy-induced mass transport from our eddy fluxes (see discussion in Lu et al., 2022; Lu & Kamenkovich, 2025). The latter eddy mass transport is a different mechanism of tracer transport that is traditionally parameterized using Gent-McWilliams formulation (Gent et al., 1995; Gent & McWilliams, 1990). In other words, the total mass flux, $\langle \overline{\mathbf{u}h} \rangle$, is assumed to be known. Note also that we used

the simple average of tracer concentration $\langle \overline{c} \rangle$ rather than the layer-thickness weighted average $\langle \overline{hc} \rangle / \langle \overline{h} \rangle$ in Equation 5. We confirmed that the relative difference between $\langle \overline{c} \rangle$ and $\langle \overline{hc} \rangle / \langle \overline{h} \rangle$ is less than five percent across the domain.

The Moore-Penrose pseudoinversion (denoted by superscript †) is used to invert the tracer gradients since more than two tracers are used in this study. The angle brackets denote 120 km × 120 km coarse-graining operator (i.e., spatial average over all fine-grid cells within a coarse cell of 120 km × 120 km; see Mana and Zanna (2014) for details), and the overbar stands for the 2-year time average. Therefore, the eddies in this study are motions with length scales shorter than about 120 km but does not include submesoscale eddies due to the limited spatial resolution and adiabatic configuration of the model. The use of the combination of spatial and long-term time averaging to define the large-scale components is to remove the mesoscale variability, which is more effective than, for example, spatial or time averaging alone (Kamenkovich & Garraffo, 2022; Lu & Kamenkovich, 2025). Lu and Kamenkovich (2025) verified that the results are not sensitive to the averaging as along as the averaging window is longer than the time scale of mesoscale eddies. The Eulerian tensor $\mathbf{K}^E$ in this definition depends on location but is constant in time.

The $\mathbf{K}^E$ tensor can be separated into the symmetric and antisymmetric parts that represent two physically distinct transport processes: the diffusive and advective effects, respectively (Griffies, 1998; Haigh et al., 2021a, 2021b). In this study, we focus on the diffusive component, which represents mixing and directly affects global tracer variance. The diffusive tensor can also be estimated asymptotically from the spread/dispersion of Lagrangian particles (e.g., I. Rypina et al., 2011) (see Introduction). Although our main focus is on the local Eulerian diffusivity and its spatial variability, we also estimate the Lagrangian (nonlocal) diffusivity. The results exhibit substantial differences with the Eulerian estimates; see Appendix B for brief results and discussion. Notably, the asymptotic Lagrangian diffusivity has large-scale, smooth spatial structure and is always positive in both major and minor directions, while the Eulerian counterpart tends to have pairs of opposite signs, so-called "polarity" (Haigh & Berloff, 2021; Kamenkovich et al., 2021; Lu et al., 2022). These differences are not surprising, since the Lagrangian diffusivity is not designed to approximate the local Eulerian one in an inhomogeneous and non-stationary flow. Also, the Lagrangian diffusivity contains no information at all on tracer concentration, whereas the Eulerian one depends on it. Investigating the difference between the two methods is beyond the scope of our study. Here we focus on using the Lagrangian particles to generate local and transient estimates of the Eulerian diffusivity and its spatial and temporal variability.

The diffusion tensor $\mathbf{S}$ can be further diagonalized:

$$\mathbf{S} = \begin{pmatrix} S_{11} & S_{12} \\ S_{12} & S_{22} \end{pmatrix} = \mathbf{I}_R \begin{pmatrix} \lambda_1 & 0 \\ 0 & \lambda_2 \end{pmatrix} \mathbf{I}_R^T, \tag{6}$$

where

$$\mathbf{I}_R = \begin{pmatrix} \cos\theta & -\sin\theta \\ \sin\theta & \cos\theta \end{pmatrix} \tag{7}$$

is the rotation matrix, the diffusion angle θ defines the direction of the maximal diffusion, and $\lambda_{1,2}$ are the corresponding eigenvalues (diffusivities). We define λ_1 as the largest diffusivity and λ_2 as the smallest one. Hereafter, we refer to λ_1 and λ_2 as the "major" and "minor" diffusivity, respectively. λ_1 and λ_2 have been shown to be generally different, resulting in the anisotropy in eddy diffusion (Bachman et al., 2020; Haigh & Berloff, 2021; Kamenkovich et al., 2021; Lu et al., 2022; Zhang & Wolfe, 2022).

The Equation 4 can be solved exactly for each given pair of tracers, but the tensor in this case depends on initial distribution of tracers, which makes the solution nonunique (e.g., Kamenkovich et al., 2021; Sun et al., 2021). An alternative approach is to minimize the tracer dependence by using a large number of tracers (e.g., Abernathey et al., 2013; Bachman et al., 2020; Lu et al., 2022). Following this approach, we solve the overdetermined problem $\mathbf{K}^E$ in Equation 4 with the eight linearly independent tracers (Appendix A). The tensor is calculated by the Moore-Penrose pseudoinverse with a least-squares approximation. Note that in this case the flux-gradient relation

becomes approximate rather than exact, that is, the resulting tensor approximately reconstructs the eddy tracer fluxes.

2.4. Hybrid Eulerian-Lagrangian Estimate of the Diffusivity Tensor

Applications of the flux-gradient relationship Equations 4 and 5 using multiple tracers are challenging in practice. High-resolution simulations with multiple tracers are computationally expensive. In the real ocean, implementing the multiple-tracer approach is prohibitively complex and costly. In addition, the variations of layer thickness are generally not available from observations.

In this study, we explore a hybrid Eulerian-Lagrangian method of calculating Eulerian diffusivity using Lagrangian trajectories and velocities. Due to the unavailability of layer thickness in observations, our target hybrid diffusivity is slightly different from the isopycnal formalism (Equation 4) and is defined without including layer thickness variations:

$$\mathbf{K}^H = -F^H_{i\beta}[\partial_j\langle\overline{c}_\beta\rangle]^\dagger, \tag{8}$$

where the eddy flux is computed without layer-thickness-weighted averaging

$$F^H_{i\beta} = \mathbf{F}^H_e = \langle\overline{\mathbf{u}c}\rangle - \langle\overline{\mathbf{u}}\rangle\langle\overline{c}\rangle, \tag{9}$$

and other symbols and notations are the same as Equation 4. The hybrid approach will use Lagrangian trajectories to estimate the tracer flux $\mathbf{F}^H_e$ and tracer concentration. We confirm that excluding the layer-thickness-weighted averaging in the hybrid estimate does not change the results and the difference between the Eulerian and hybrid estimates are not due to the layer-thickness-weighting.

The key idea here is that fluid motion can be described by a finite number of fluid particles (Sebille et al., 2018; Wagner et al., 2019), which are viewed as fluid parcels with specific volumes and tracer contents (Haine et al., 2025; Holzer & Hall, 2000). We carry out the calculations on the same coarse grid as is used in the Eulerian method. Specifically, we assign each particle originating from a 120 km × 120 km bin with the bin's initial tracer concentration. We let the particles conserve their volume and tracer content, which means that, unlike the continuous Eulerian estimate in Section 2.3, small-scale mixing of the tracer properties between water particles and surrounding water is neglected. At each time t, the bulk tracer concentration $\langle c\rangle_{bn}$ in a bin "bn" is estimated as an average of the tracer content of $N_{bn}(t)$ particles contained in this bin:

$$\langle c\rangle_{bn}(t) = \frac{\sum c_l}{N_{bn}(t)}, \tag{10}$$

where the subscript l stands for the indices of the particles in the bin "nb," the summation $\sum$ is performed over particles found in the bin at t, and $N_{bn}(t)$ is the number of particles in the $(120\ \text{km})^2$ bin. If a bin does not contain any particles, the tracers in those bins are set to missing values, although the number of particles used here (∼1 mil) is large enough to ensure all bins are sampled.

The Lagrangian velocities $\mathbf{u}_l$ along particle trajectories can then be used to estimate the large-scale Eulerian velocity:

$$\langle\mathbf{u}\rangle_{bn}(t) = \frac{\sum \mathbf{u}_l}{N_{bn}(t)}. \tag{11}$$

Similarly, the large-scale tracer flux is calculated by:

$$\langle\mathbf{u}c\rangle_{bn}(t) = \frac{\sum \mathbf{u}_l c_l}{N_{bn}(t)}. \tag{12}$$

The Equation 5 then becomes

$$\mathbf{F}_e = \overline{\langle \mathbf{u}c \rangle_{bn}(t)} - \overline{\langle \mathbf{u} \rangle_{bn}(t)}\,\overline{\langle c \rangle_{bn}(t)}. \tag{13}$$

The particle-based large-scale tracer concentration $\langle c \rangle_{bn}$, velocity $\langle \mathbf{u} \rangle_{bn}$ and tracer flux $\langle \mathbf{u}c \rangle_{bn}$ fields are then used to calculate the hybrid Eulerian-Lagrangian diffusivity tensor $\mathbf{K}^H$ using Equation 4. Zonal and meridional fluxes and tracer gradients in Equations 11 and 12 are diagnosed on the staggered u- and v-grid bins, respectively. To isolate errors associated with the new Lagrangian approach and minimize purely numerical errors, we compute the Lagrangian velocity $\mathbf{u}_l$ by interpolating the fine-scale Eulerian velocity field to the exact particle positions, rather than by differentiating particle trajectories. Although the latter method is more relevant to real-ocean applications, it can introduce additional errors in this study that uses time- and spatial interpolation to calculate trajectories from velocities that were saved every 6 hr.

A key characteristic of the new method is the dependence of its accuracy on the average spacing between particles, or, equivalently, on the "Lagrangian resolution." What is the lowest resolution that still yields an acceptable accuracy of the hybrid estimate for the given eddy scale? To address this question, we used ensembles of particles with progressively reduced particle resolutions and calculated $\mathbf{K}^H$ from each of them. These ensembles are generated by randomly subsampling the original set of 1,048,576 particles (initially spaced 3.75 km apart), with each ensemble consisting of 10 members. Each ensemble member contains the same total number of particles, differing only in their initial positions. We define the measure of the average spacing between particles, that is, the "Lagrangian resolution," as

$$\Delta x_l = \frac{120\,\mathrm{km}}{\sqrt{N_{bn}}}, \tag{14}$$

which can be interpreted as "one particle per Δx_l." The "120 km" is the width of the coarse bin.

We used here four "reduced-resolution" particle ensembles:

- "RR1/8": initially 131 072 particles (1/8 of the number of particles of the original set); the Lagrangian resolution $\Delta x_l \approx 11$ km ($N_{bn} = 128$).
- "RR1/32": initially 32 768 particles (1/32 of the original set); $\Delta x_l \approx 21$ km ($N_{bn} = 32$).
- "RR1/128": initially 8 192 particles (1/128 of the original set); $\Delta x_l \approx 42$ km ($N_{bn} = 8$).
- "RR1/512": initially 2 048 particles (1/512 of the original set); $\Delta x_l \approx 85$ km ($N_{bn} = 2$).

Figure 2 shows the Lagrangian resolutions Δx_l in different ensemble experiments estimated from the time-mean number of particles. The resolution is not spatially uniform due to the convergence/divergence of the current and reflects key features of the circulation. In all experiments, Δx_l is relatively short (higher resolution, more particles) to the south of the jet, probably because of the recirculation that traps particles in that region. The resolution is always lower near the western boundary and to the north of the jet than in other regions. This is likely to be explained by a strong eastward jet moving particles away from this region a weak supply of particles from the north. The time-mean area-averaged Δx_l is very close to the initial Lagrangian resolution (not shown), indicating that the loss of particles due to their disappearance at the boundary is negligible.

For each ensemble member at various Lagrangian resolutions (RR1/8 to RR1/512), we calculate the corresponding Eulerian-Lagrangian estimates of the large-scale tracer and fluxes based on Equations 10–12, as well as the hybrid eddy diffusivity tensor $\mathbf{K}^H$. Then, for each ensemble, we calculate the ensemble means and standard deviations of these quantities.

3. Results

We first compare the hybrid and Eulerian estimates of the tracer concentrations, eddy fluxes, and diffusivities in Section 3.1. We then provide an explanation of the difference between the hybrid and Eulerian estimates in Section 3.2. In Section 3.3, we repeat the analysis for a regional study where particles are released only in the vicinity of the eastward jet.

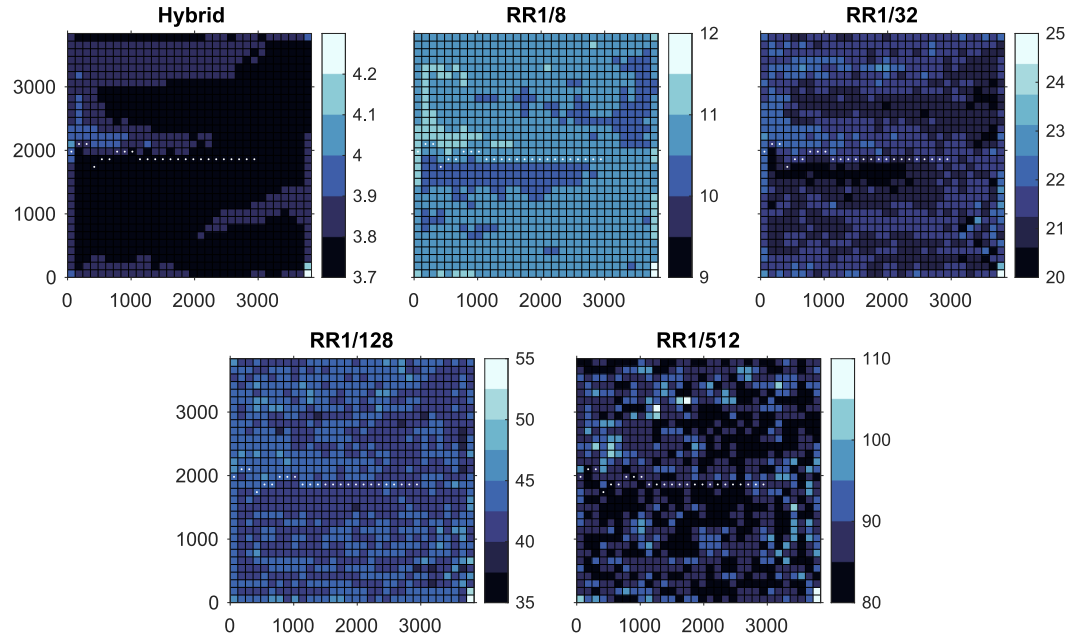

Figure 2. "Lagrangian" resolutions Δx_l [km] (Equation 14) for different particle release experiments. It is derived from the 2-year averaged number of particles per bin (120 km × 120 km). White dots are the eastward jet core defined by the maximal speed of the coarse-grained velocity.

3.1. Eulerian and Hybrid Estimates

We start by comparing the particle-based estimates of the tracer concentrations and tracer fluxes to those directly diagnosed from the model ("Eulerian"). Note, however, that the Eulerian tracer concentrations are affected by explicit subgrid mixing and numerical dispersion that do not affect the particle-based estimates. Eulerian estimates also account for layer thickness variations that are not available in Lagrangian data. An example of instantaneous maps of these fields are shown in Figure 3. The visual inspection shows the overall similarity between the particle-based estimates and the actual Eulerian fields, even in a largely reduced-resolution case RR1/128 ($\Delta x_l = 42$ km). As the Lagrangian resolution decreases to 85 km (RR1/512), however, the errors in the tracer and tracer flux fields become more pronounced. The errors grow particularly fast at those locations where the particles are spreading away, further degrading the local Lagrangian resolution (Figure 2) and leaving too few particles to give accurate estimates of the Eulerian fields. For example, in experiment RR1/512, the errors in tracer concentrations are particularly large to the north of the eastward jet. This is also the region where the Lagrangian resolution is lower compared to the rest of the domain.

To quantify the difference of the hybrid estimates of tracer gradients and fluxes relative to the Eulerian ones, we calculate the relative error between two vectors as:

$$Er = \frac{\left\| \mathbf{V}^H - \mathbf{V}^E \right\|}{RMS\left(\left\| \mathbf{V}^E \right\| \right)}, \tag{15}$$

where the vector $\mathbf{V}$ represents either the large-scale tracer gradient, tracer flux, or the eddy flux, the superscript "E" denotes the fields from the Eulerian model and "H" denotes the hybrid estimates. The denominator is the domain root mean square value of the Eulerian vector norm to avoid division by near-zero local values in the vector norms. Since the Eulerian tracer flux and eddy tracer flux are thickness weighted while their hybrid counterparts are not, we normalized the Eulerian fluxes by layer thickness when calculating the Er (see caption of Figure 4). Figure 4a shows the domain median values of Er for the tracer gradient as a function of time. The errors in tracer gradients and fluxes become saturated after the first 200 days, except for the RR1/512 that continues to

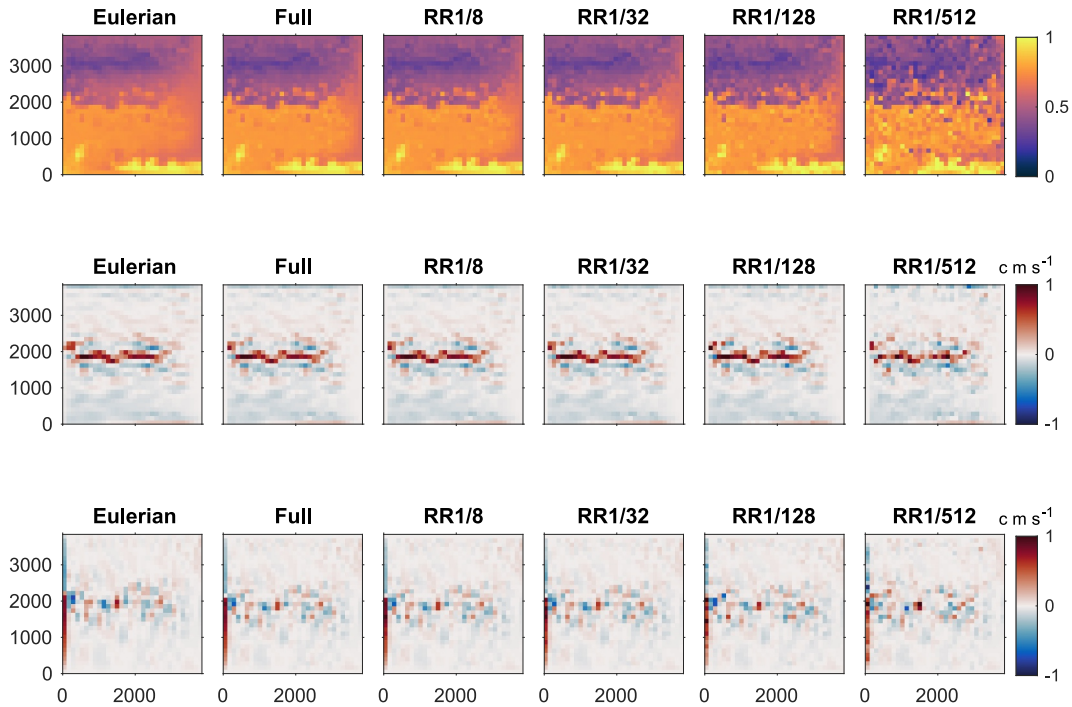

Figure 3. (Top) Large-scale tracers $\langle c \rangle$ derived from the model ("Eulerian"), and from the hybrid estimates using the complete particle set ("Full," $\Delta x_l = 3.75$ km) and the four subsampled particle ensembles. (Middle) Zonal components of the large-scale tracer fluxes $\langle uc \rangle$. (Bottom) Meridional components of the large-scale tracer fluxes $\langle vc \rangle$. All fields are diagnosed at day 730 in the upper layer, and are for the tracer c_1 (Appendix A). Other tracers have similar results. Note that for the subsampled cases, the fields from one particle set in each ensemble, instead of the ensemble mean, are plotted. The large-scale tracer flux in the "Eulerian" case is divided by layer thickness ($\langle \mathbf{u}hc \rangle / \langle h \rangle$) to have the consistent unit.

grow over the whole time period. They also decrease as the Lagrangian resolution increases. Importantly, the errors for the ensembles RR1/8 and RR1/32 are very close to the errors for the original particle set (Full). This indicates that increasing the Lagrangian resolution (i.e., the number of particles) from 21 km (RR1/32) to 3.75 km (Full) results in very small gains in the accuracy of the hybrid estimates, suggesting convergence toward an asymptotic regime at a resolution of approximately <=21 km. This can be further seen from the errors in the time-mean tracer concentration gradients as a function of different Lagrangian experiments (Figure 4b): the errors start to increase from "RR1/128" ($\Delta x_l = 42$ km) to "RR1/512" ($\Delta x_l = 85$ km). Similar results are seen for the hybrid estimates of the time-dependent tracer flux $\langle \mathbf{u}c \rangle_{bn}$ (Figure 4c) and time-invariant eddy fluxes $\mathbf{F}_e^H$ (Figure 4d). One thing to notice is that the increase in the magnitude of errors in tracer gradients (Figure 4b) with coarser Lagrangian resolution is steeper than for the errors in eddy fluxes (Figure 4d). This result implies that the tracer and its gradients are more sensitive to the number of particles than are the tracer fluxes. This is mainly due to small tracer gradients in the well-mixed regions of the domain, resulting in large relative errors. In short, the hybrid estimates of tracer gradients and tracer fluxes are reasonably accurate for Lagrangian resolutions finer than ~21 km which is equivalent to having one particle per shortest length scale simulated by the model. In the real ocean similar resolution for Lagrangian data could be achieved in such a regional drifter experiment as the Lagrangian Submesoscale Experiment (LASER; Balwada et al., 2022; D'Asaro et al., 2018). During that experiment, ~1,000 drifters were released in the Gulf of Mexico ($\sim 1.6 \times 10^6$ km^2), giving an average Lagrangian resolution of 40 km under the assumption of uniform coverage. In reality, the LASER drifters achieve a finer effective resolution because sampling occurred only within a portion of the Gulf. This shows that the "optimal" Lagrangian resolution identified in our model is comparable to the resolution of drifter observations, supporting the applicability of our hybrid approach.

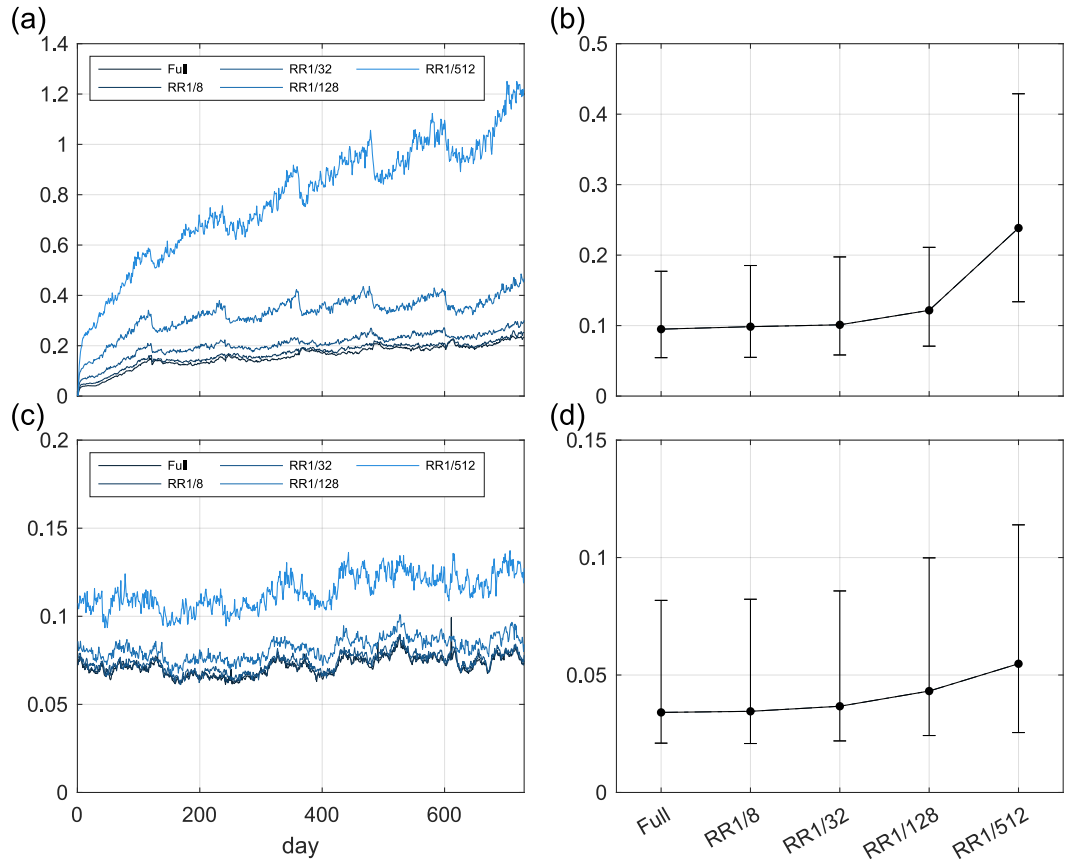

Figure 4. (a) Domain median values of the relative errors Er in the instantaneous large-scale tracer concentration gradients from the hybrid estimates; x-axis is the time. (b) Domain median values of the relative errors between the time-mean tracer gradients $\nabla\langle\overline{c}\rangle$; x-axis is the particle experiments. Bars denote the 25th and 75th percentiles. (c) Same as (a) but for the instantaneous large-scale tracer fluxes $\langle \mathbf{u}c\rangle_{bn}$. The Eulerian tracer fluxes is defined as $\langle \mathbf{u}hc\rangle/\langle h\rangle$. (d) Same as (b) but for the (time-invariant) eddy tracer fluxes $\mathbf{F}_e^H$. The Eulerian eddy tracer fluxes is divided by the time-mean layer thickness $\left(\mathbf{F}_e^E/\langle\overline{h}\rangle\right)$ to make the units consistent.

To further confirm that the Lagrangian resolution in Full is indeed sufficient for our purposes, we performed an additional simulation with 1,048,576 particles with different initial positions from the particles in Full, and combined the results with the Full simulation, thus doubling the total number of particles. We then used the total ~2 million particles ($\Delta x_l = 1.875$ km) to estimate the diffusivity using the hybrid approach. The resulting diffusivity is almost identical to that from Full which is not shown. This confirms that the differences between Full and Eulerian are not due to insufficient Lagrangian resolution.

We next compare the Eulerian and hybrid eddy diffusivity tensors. Their major and minor diffusivity eigenvalues $\lambda_{1,2}$ and the direction of maximal diffusion, angle θ, are shown in Figure 5. Both eigenvalues of the Eulerian diffusivity tensor $\mathbf{K}^E$ have large magnitudes near the jet. The major diffusivity is always positive, and is primarily directed along the jet stream, as indicated by the map of θ. This is mainly due to the shear dispersion caused by the mean flow (e.g., Young et al., 1982; Zhang & Wolfe, 2022). The minor diffusivity is, however, mostly negative, indicating a persistent upgradient eddy flux in the direction normal to the jet axis (Haigh & Berloff, 2021; Haigh et al., 2021b; Kamenkovich et al., 2021). Such an upgradient flux is a manifestation of the eddy-induced frontogenesis in the jet region, as discussed by Lu and Kamenkovich (2025). The overall spatial distribution in hybrid estimates $\mathbf{K}^H$ (Figures 5d and 5e) from the full particle set closely resemble that of $\mathbf{K}^E$ with large values concentrating around the jet. Figures 5g and 5h further show the diffusivity estimates with reduced resolution of the particle ensemble with $\Delta x_l = 21$ km. The spatial patterns of these diffusivities are also similar to those from the Full and Eulerian experiments. Although some scattered large values, such as those in the southern domain, are

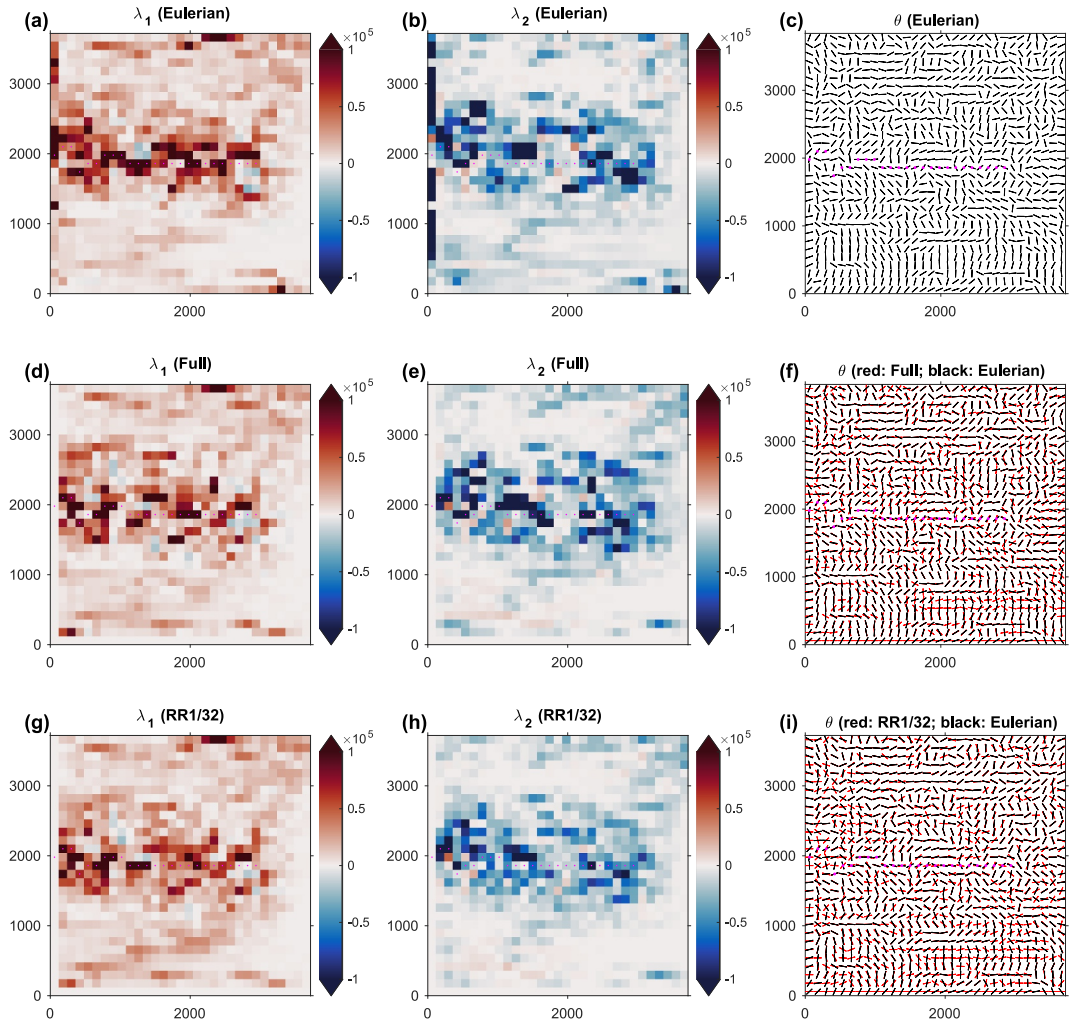

Figure 5. (a–c) The major component λ_1, minor component λ_2, and diffusion angle θ of the Eulerian diffusivity $\mathbf{K}^E$, respectively. (d–f) Same with (a–c) but for the hybrid diffusivity $\mathbf{K}^H$ from the full particle set ($\Delta x_l = 3.75$ km). (g–i) Ensemble mean of the hybrid diffusivity $\mathbf{K}^H$ from the "RR1/32" ensemble ($\Delta x_l = 21$ km). The magenta dotted line marks the eastward jet core. In (f, i), the diffusion angle of the Eulerian tensor is shown in black bars for comparison.

not captured by the reduced-resolution simulation, these spots are unlikely to be important for the large-scale tracer distribution.

The Full experiment also reproduces the spatial structure of θ well in most of the domain, although errors are still visible in several regions. For example, errors in θ are visible in the jet region, in both Full and RR1/32 (Figures 5f and 5i). Another region of relatively large errors is the southern part of the domain, although the eddy activity there is weak and eddy diffusivity is small (Figures 5a and 5b). These errors are expected since the calculation of the diffusion angle includes taking inverse tangent that is sensitive to errors in the symmetric (diffusive) off-diagonal component of the transport tensor.

To quantify the differences between the large-scale diffusivity estimates, we choose to focus on the zonally and meridionally averaged values. Figures 6a and 6b show the zonally averaged profiles of the major and minor diffusivities. Overall, all of the particle-based estimates exhibit a meridional structure similar to that of the Eulerian estimate, with large magnitudes in the vicinity of the jet and peak values at $y \sim$ 2000 km. The peak magnitudes are, nevertheless, weaker in the hybrid case than in the Eulerian: ~6.6 versus 7.7×10^4 m^2 s^{-1} for λ_1, and the largest differences are found south of $y \sim$ 2000 km. In contrast, Full, RR1/32 and Eulerian estimates are in good agreement north of $y \sim$ 2000 km. The relatively large differences in the major diffusivity component near

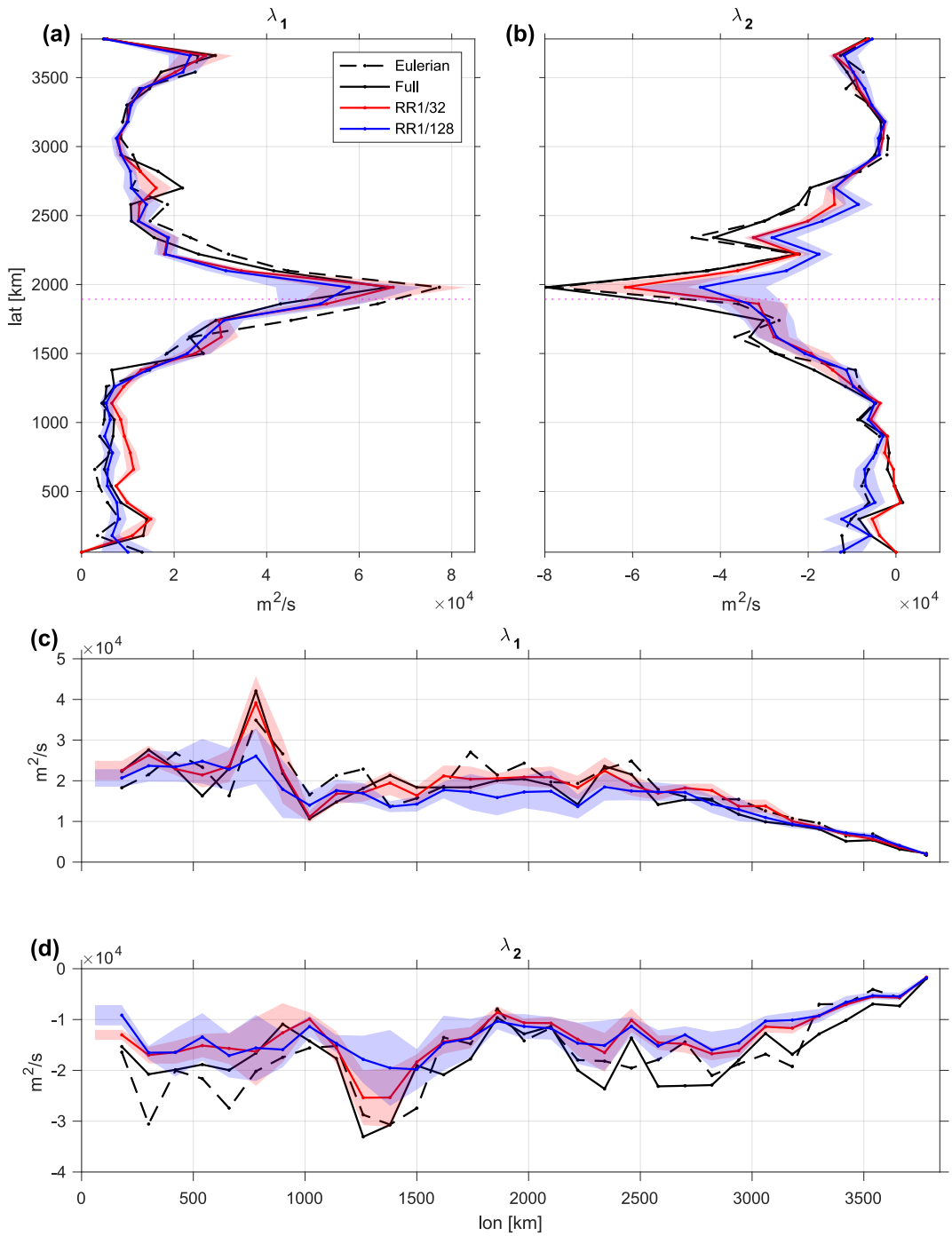

Figure 6. Zonally (a, b) and meridionally (c, d) averaged eddy diffusivities. (a, c) Major component λ_1. (b, d) Minor component λ_2. Dashed dotted lines are the Eulerian estimate $\mathbf{K}^E$. Red (RR1/32) and blue (RR1/128) lines are the ensemble-mean of hybrid estimates $\mathbf{K}^H$ from the subsampled ensembles with $\Delta x_l = 21$ km and $\Delta x_l = 42$ km, respectively. The shading denotes one ensemble standard deviation. Each ensemble has 10 members (particle sets) as described in text. The magenta dotted lines in (a, b) denote the zonally averaged latitude of the eastward jet core.

the jet axis ($y \sim$ 1900 km) can be expected due to the sharp tracer front along the jet. At the jet axis, the major diffusivity is aligned with the front and mean tracer contours, which diminishes its impact on cross-front transport and complicates the application of the flux-gradient relationship (Lu and Kamenkovich (2025)). The importance of the along-front diffusivity component for the frontogenesis is, however, unclear. Second, as discussed in Lu

and Kamenkovich (2025), the front is sustained by eddy-induced squeezing of tracer contours along the jet, which could be difficult to capture with particles since they tend to quickly move downstream and along the front and take the tracer information away from the jet region. That is, the particle density near the front decreases over time due to the strong jet, leading to deterioration of particles' ability to reproduce the sharp tracer gradient there.

The Eulerian and hybrid estimates of minor diffusivity λ_2 are in much better agreement than the major components, all exhibiting peak values at $y \sim$ 2000 km. Note that it is the diffusivity in the direction normal to the mean tracer contours—often referred to as the "effective diffusivity"—that is particularly important for the tracer distribution (Nakamura, 1996). The negative values we observe in Figure 6b are therefore indication of the formation of tracer fronts at the jet core. Figures 6c and 6d show the meridionally averaged diffusivities. The diffusivity exhibits variability that is weaker than in Figures 6a and 6b. Both λ_1 and λ_2 are larger in the west than in the east. This property reflects the influence of the energetic western boundary current and associated eddies.

The ensemble mean diffusivity estimates of RR1/32 (Δx_l = 21 km) are nearly the same as the Full for λ_1. Although the minor diffusivity λ_2 at its peak at $y \sim$ 2000 km is weaker in RR1/32 than in Full, the difference is less than 25%. In contrast, the RR1/128 experiment (Δx_l = 42 km) produces less accurate estimates of both diffusivity components, with a larger uncertainty within the ensemble (shading contours). We do not show the results from the "RR1/8" because it is nearly identical to "RR1/32," and we also do not show the "RR1/512" because the errors are too large. In short, we conclude that the Eulerian eddy diffusivity can be reasonably well estimated from particles with the Lagrangian resolution of 21 km—the scale close to the first baroclinic deformation radius at the central part of the domain (23.6 km).

3.2. Sources of the Difference Between the Hybrid and Eulerian Estimates

In this section, we aim to explain the differences between the particle-based and Eulerian estimates of tracer concentrations, eddy fluxes, and eddy diffusivity tensor, which can be inherent to the hybrid Eulerian-Lagrangian approach.

One potential cause of disagreement lies in the definitions of the particle-based tracer concentration (Equation 10) and fluxes (Equation 12), which assume that each particle conserves tracer mass along its trajectory. As discussed earlier, this approach does not include both explicit mixing and numerical dispersion of tracers in the continuous tracer budget (Haine et al., 2025). To estimate the significance of these factors for the difference between the estimates in the Full and Eulerian cases, we recalculated the hybrid estimates of tracer gradients and tracer fluxes by using the Eulerian tracer concentrations interpolated on the Lagrangian particle trajectories (experiment "Interp"). Specifically, the tracer concentrations and Lagrangian velocity of each particle (c_l and $\mathbf{u}_l$ in Equations 10–12) are obtained by interpolating the Eulerian tracer field onto the particle's position. The new tracer (Equations 10) and eddy fluxes (Equation 12) are then used to re-calculate diffusivity. The Interp simulation accurately produces the tracer gradients and eddy fluxes with domain-median relative errors (Er, Equation 15) of about 0.005 and 0.02, respectively. The diffusivity λ_1 derived from Interp is nearly the same as the Eulerian one at the jet ($y \sim$ 1900 km), eliminating most of the biases in this region in the Full simulation. This implies that most of the differences between the Hybrid and Eulerian cases at the jet axis are due to errors in particle-based estimates of tracer concentrations. Note, however, that there are errors in the latitudinal position of maximal diffusivity, which is at $y \sim$ 2000 km in these simulations.

Since tracer concentration errors affect both tracer gradient and flux accuracy, we can ask how much each of these variables contributes to diffusivity errors. For this purpose, we next use the interpolated tracer values in either gradient or eddy fluxes but not both. The experiments are called "Interp—c only" and "Interp—flux (u*c) only" respectively. We see that the diffusivity derived from the "Interp—c only" case (Figure 7, magenta line) is closer to the Interp case, whereas the "Interp—flux (u*c) only" results are nearly indistinguishable from Full (meaning no improvement). We can conclude that the main cause of disagreement between Full and Eulerian south of y = 2000 km is the errors in the hybrid estimates of tracer gradient. This is expected since the diffusivity is proportional to the inverse of large-scale tracer gradient (Equation 4), and a small error in it in regions of well-mixed tracers could lead to large errors in the diffusivity.

One of the main differences between the Eulerian and hybrid estimates is the absence of thickness weighting in the latter. To assess the importance of this factor, we also computed the Eulerian values without weighting. These

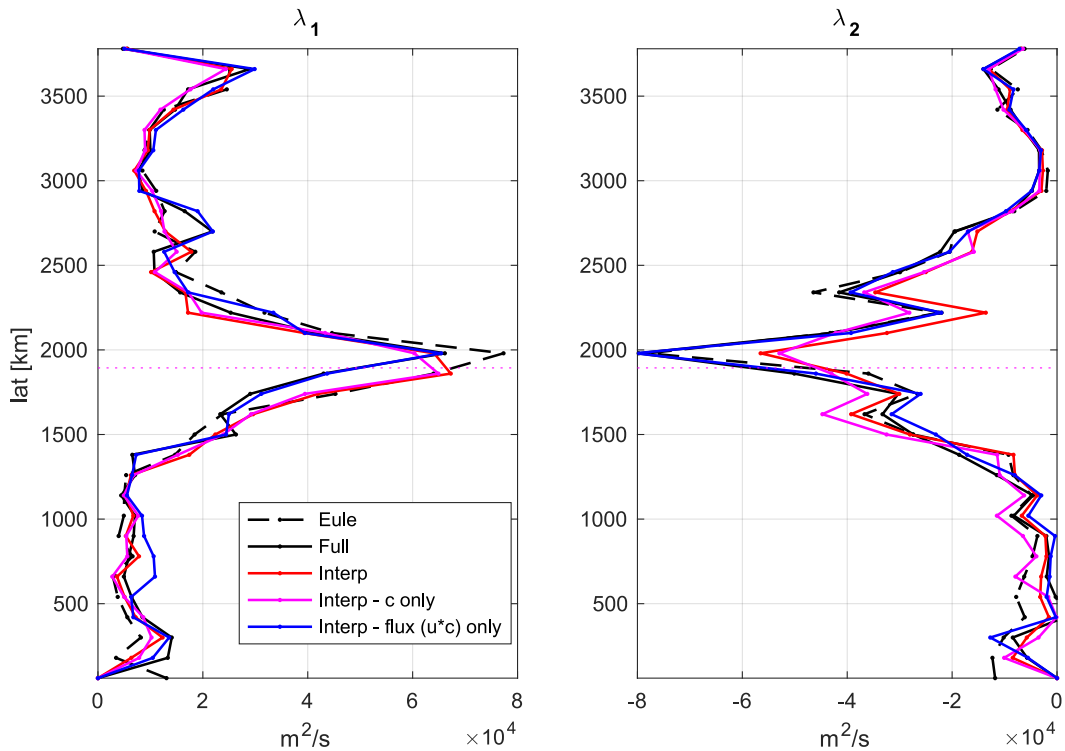

Figure 7. The major (left) and minor (right) components of the zonally averaged eddy diffusivities. "Interp": diffusivity $\mathbf{K}^H$ calculated from the particle-based tracer concentration and flux that are both derived by assigning particles with the interpolated tracer content. "Interp—c only": only tracer field is interpolated, while the tracer flux is calculated in the same way as the "hybrid" using Equation 12. "Interp—flux (u*c) only": only tracer flux field is interpolated, while the tracer is calculated in the same way as the "Full" using Equation 10. The magenta dotted lines mark the eastward jet core.

values (not shown) do not move closer to the hybrid estimates, indicating that variations in layer thickness cannot account for the discrepancy between the Eulerian and hybrid approaches.

In short, we argue that the difference between the Full and Eulerian estimates is mainly due to the particle-based simulation of the large-scale tracer gradient. Additional technical factors include the offline integration of particles' trajectories (Jiang & Haine, 2025b).

3.3. Regional Hybrid Estimates

Up to this point, we discussed the hybrid estimates that are based on the particles initially placed across the whole domain. From a practical point of view, this setting may not be realistic for the real ocean given the large amount of particles needed and their broad coverage of space. To see how our hybrid approach can be potentially applied to a more realistic regional setting, we next use only the particles released within the jet region to re-derive the hybrid estimates of tracer, tracer flux and eddy diffusivity (denoted as "Full-reg"). Note that we expect the estimates to be less accurate than in the Full simulation, as the regionally released particles lack information about tracers initially located outside the region and many also leave the jet region reducing the coverage. The regional experiments in this section aim to estimate the size of the area where the estimates are accurate and assess the importance of particles originating outside of the particle deployment region. For the sake of brevity, we focus here on the diffusion tensor only.

Figures 8a–8c show the major, minor components, and the diffusion angle of the diffusivity tensor from the new "Full-reg" simulation, where the dashed rectangle denotes the region where particles are placed initially. The Lagrangian resolution is initially 3.75 km in the rectangular region. The spatial distributions of $\lambda_{1,2}$ are in a reasonable agreement to the Eulerian and Full hybrid estimates (Figure 5). As in the previous analysis, we also subsampled the particles released from the jet region in the same way as earlier: experiments "RR1/32-reg" and "RR1/128-reg." In agreement with the earlier analysis in the entire domain, the spatial distribution of $\lambda_{1,2}$ become

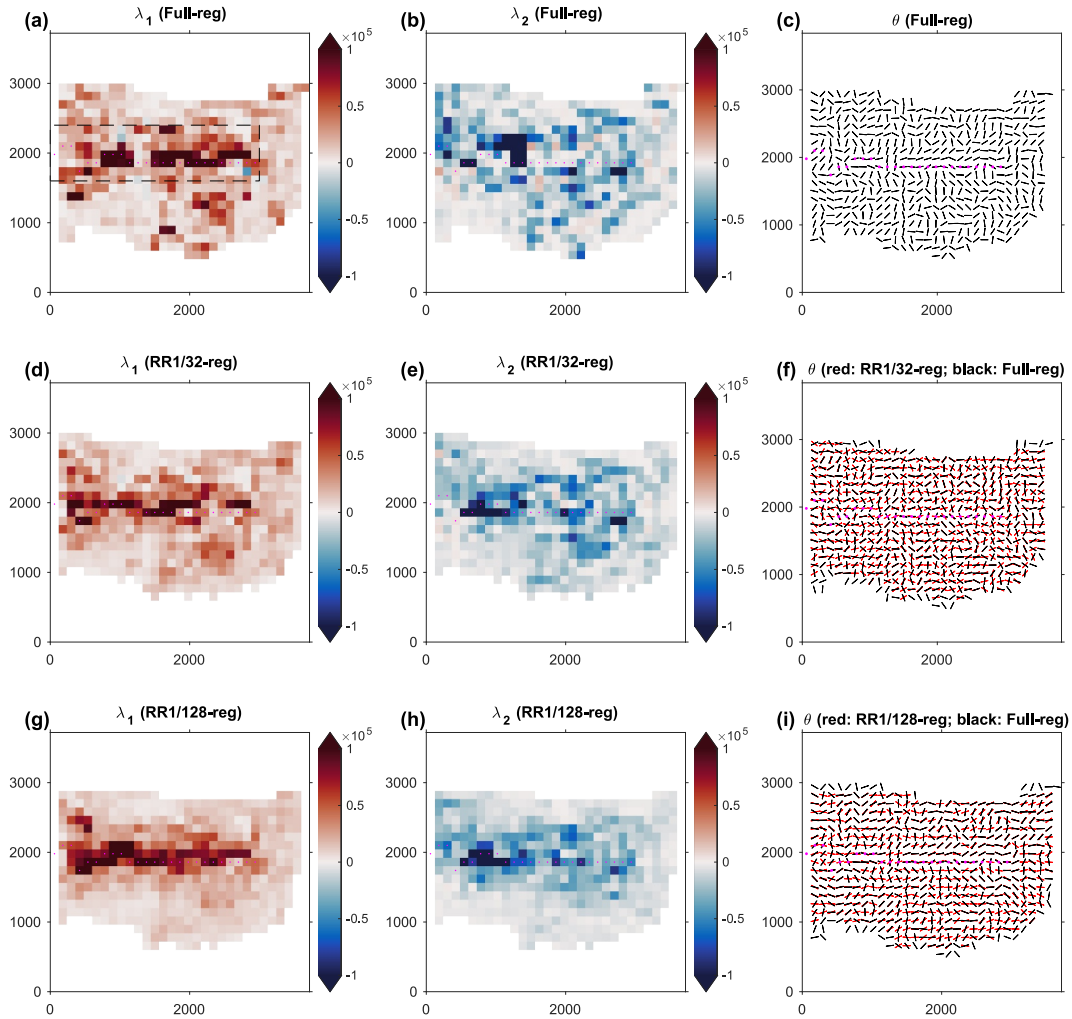

Figure 8. Same as Figure 5, but for the hybrid diffusivity estimate using only particles released in the jet region (denoted by the black dashed rectangle in (a), $0 < x < 3{,}000$ km, $1{,}600 < y < 2{,}400$ km). Missing values in the northern and southern regions are due to the lack of adequate sampling by particles.

smoother and their magnitudes become weaker, as the Lagrangian resolution decreases (Figures 8d–8i). The diffusion angles become less accurate (e.g., Figure 8i) and more zonal as the Lagrangian resolution decreases.

Zonally averaged profiles of the major and minor diffusivity components provide a more quantitative comparison (Figure 9). The major component from the Full-reg simulation is very close to the Eulerian north the jet core (1,900 km) and overestimates the λ_1 south of the jet axis. The minor component of Full-reg significantly underestimates the peak values near the jet core. The ensemble-mean λ_1 of RR1/32-reg is similar to the RR1/32 from the full-domain release but very different from Full-reg and Eulerian. Unexpectedly, the ensemble-mean λ_1 from RR1/128-reg is closer to the Eulerian estimate even than is the RR1/32-reg south of the diffusivity peak ($y \sim 2000$ km), although the uncertainty in the estimate, defined by the ensemble s.t.d., in RR1/128-reg is large. For λ_2, both the RR1/32-reg and RR1/128-reg estimates peak south to the maximum value in Eulerian. As discussed earlier, the increased bias in the regionally released experiments is due to the lack of particles originating from the outside of the release region leading to missing information of tracer evolutions.

Despite the increased biases, the regionally released particles can still provide reliable estimates of the major and minor components of the Eulerian eddy diffusivity in most of the region. This implies a broader application of our hybrid approach to estimate Eulerian fields.

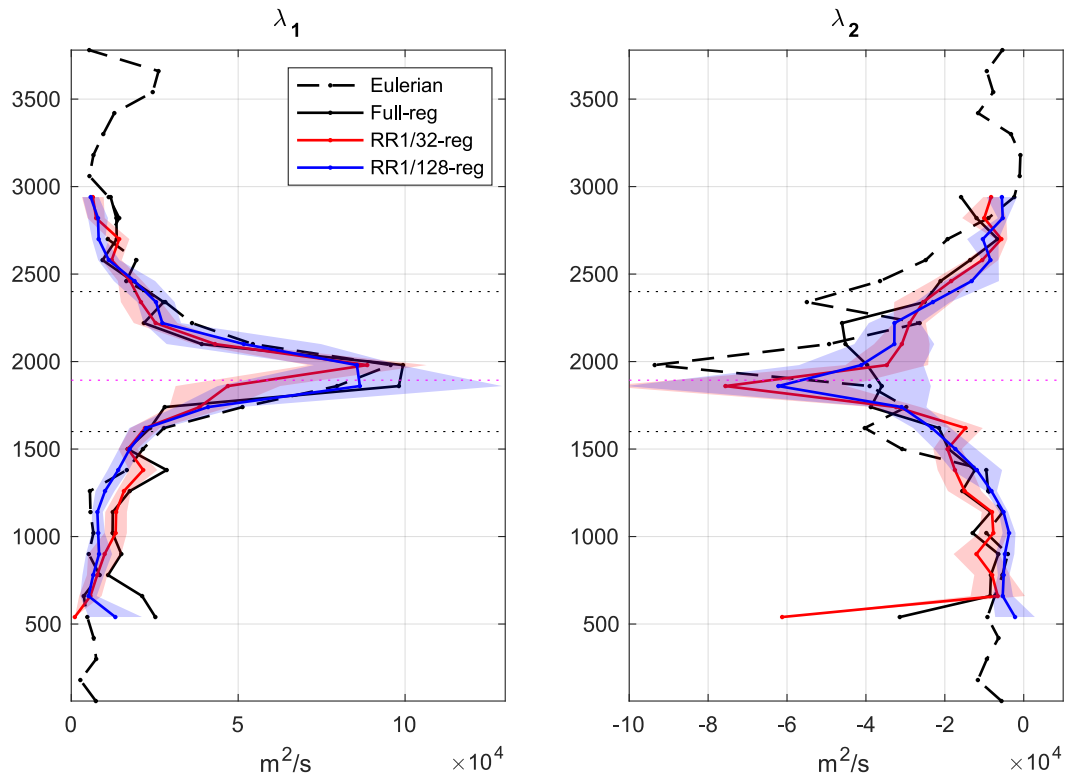

Figure 9. The major (left) and minor (right) eddy diffusivities. The hybrid estimate diffusivities are estimated using particles released in the jet region (bounded by the horizontal dotted lines). Note that the zonal average here is performed for the points in the range of $0 < x < 3{,}000$ km, which is the jet region defined in Figure 8, so the "Eulerian" profiles are slightly different from those in Figure 8. The magenta dotted line denotes the jet core. The zonal mean profiles of diffusion angle θ are not shown due to relatively large errors.

4. Conclusion and Discussion

In this work, we use numerical simulations with synthetic Lagrangian particles and idealized tracers to estimate the Eulerian eddy diffusivity tensor. We propose a novel hybrid Eulerian-Lagrangian approach, which calculates tracer concentrations, eddy tracer fluxes, and Eulerian eddy diffusivity directly from Lagrangian trajectories. The goal is to capitalize on the strengths of the Eulerian and Lagrangian techniques by blending these two approaches. Our motivation stems from the fact that the local Eulerian eddy diffusivity is most directly applicable to eddy parameterizations in ocean models. At the same time, Lagrangian methods for estimating ocean properties are often more practical than tracer-based approaches—both in the real ocean, where they rely on particle trajectories rather than complex multi-tracer releases, and in numerical simulations, where they are more numerically efficient and are less susceptible to numerical errors. For example, Lagrangian trajectories need to be calculated in a model or measured in the ocean only once, but can then readily generate simulations of large tracer ensembles. The main objective of the study is to explore to what extent the Lagrangian trajectories can be used to produce accurate Eulerian estimates of eddy transport and diffusivities.

Like the traditional tracer-based method, the new hybrid approach is also based on the flux-gradient relation. The key difference is that the tracer concentrations, eddy velocities and eddy fluxes are all calculated from Lagrangian particle trajectories and velocities. Using an idealized shallow-water model of the double-gyre flow, we release synthetic particles that are evenly distributed across the model domain, and assign each particle with its own tracer content. Once the trajectories are known, tracer distributions over time can be then estimated offline from any given initial tracer concentrations, which makes it particularly numerically efficient. The Eulerian tracer and eddy flux fields are derived by using particles and their "assigned" tracer contents in each bin on a coarse numerical

grid, and at every time step. The Eulerian eddy diffusivities are finally calculated using the large-scale tracer concentrations and eddy fluxes by inversion of the flux-gradient relation.

The results demonstrate that the tracer concentrations, eddy fluxes and eddy diffusivities estimated by the new method are very close to those calculated from continuous Eulerian tracers. The major (along-stream) and minor (cross-stream) components of the Eulerian eddy diffusivity show maximum values near the northern part of the eastward jet extension, but they have opposite signs. This combination of major and minor diffusivities signifies the eddy-induced frontogenesis (Lu & Kamenkovich, 2025), although the cross-frontal ("effective") diffusivity can be expected to be most important for large-scale tracer distribution. The particle-based method can capture this structure well even when the Lagrangian resolution of particles is decreased to about $\Delta x_l = 21$ km, which is close to the first internal deformation radius in the model. This demonstrates the effective capacity of Lagrangian particles to estimate Eulerian eddy transport fields. The estimated minimal Lagrangian resolution depends on the length scale of eddies, which is shown to be shorter than about 120 km in this study. We therefore expect the minimal resolution to be finer for shorter length scale of motions represented by the hybrid diffusivity. For example, diffusivity parameterizing submesoscale motions will require much denser particle coverage than that suggested by this study.

Our further analyses show that the remaining differences between the Eulerian and hybrid estimates of eddy diffusivity are mainly due to biases in the hybrid estimates of tracer gradients, especially in the along-front (major) direction where these gradients are weak. Such biases could be traced to the definition of the particles' tracer contents and the inherent difference between the Lagrangian and Eulerian methods, such as the explicit and numerical mixing in the Eulerian simulations. We, therefore, argue that the difference between the Lagrangian and Eulerian methods cannot be fully eliminated due to technical constraints such as the finite number of particles and time steps in the trajectory integration. It is not, however, obvious which of these estimates is most relevant to parameterizing eddy mixing in non-eddy-resolving models.

The proposed hybrid Eulerian-Lagrangian approach can be applied to real-ocean Lagrangian drifters/floats, leading to reliable estimates of eddy fluxes and local Eulerian eddy diffusivities. From continuous drifter trajectories, one can derive Lagrangian velocities by differentiating positions, assign synthetic tracer contents corresponding to idealized realizations, and obtain tracer fields, eddy tracer fluxes, and Eulerian eddy diffusivity. Such local diffusivity estimates are essential for strongly inhomogeneous flows and cannot be obtained from asymptotic, and thus non-local, dispersion-based estimates. One potential difficulty is that the drifter observations in the global ocean have fewer counts and coarser Lagrangian resolutions (see global maps of the count in Brolly, 2023; Laurindo et al., 2017). Regional applications of our approach are more promising, because they could afford a large number of observations at finer Lagrangian resolution, such as the LASER experiment (D'Asaro et al., 2018) discussed in Section 3.1. The results from our experiments with a regional particle release demonstrate that our approach can indeed be applied to the regional Lagrangian measurements, despite the fact that the sampling coverage tends to deteriorate over time leading to increasing uncertainty in the results. Testing in realistic models and using real-ocean observations are clearly needed in future studies.

One limitation of this work is the lack of temporal variability of the diffusivity, which is not discussed in this study based on time-mean eddy fluxes and tracer gradients. The transient eddy fluxes can be significantly correlated with transient tracer anomalies, causing long-term large-scale effects such as frontogenesis (Lu & Kamenkovich, 2025). Recently, Qian et al. (2022) proposed new formulation to define the diffusivity in a localized and instantaneous sense, and Liu et al. (2024) applied it to study the irreversible mixing induced by geostrophic eddies over the global ocean. Their formulations successfully reconciled the Lagrangian, effective and Osborn–Cox diffusivity, but did not consider the Eulerian diffusivity discussed in this study. A relation between their formulation and Eulerian diffusivity tensor can be a subject of a future study. Note that examination of time-dependent eddy fluxes may, for example, lead to higher sensitivity of the estimates to particle resolution.

An important driver of eddy mixing in the upper ocean not discussed here is submesoscale currents, which need to be accounted for in real-ocean application of our approach. Submesoscale currents are missing in our study but can cause strong convergence/divergence of drifters (D'Asaro et al., 2018) due to the associated vertical motions. The resulting aggregation of particles into some places can reduce the Lagrangian resolution in other places. Studies of how these small-scale currents affect the hybrid approach should clearly be performed, as they are needed for providing guidance on how real-ocean observations are deployed.

As shown in this and other studies (e.g., Haigh et al., 2020; Kamenkovich et al., 2021), Eulerian eddy diffusivity can be negative under many circumstances, posing challenges for eddy parameterizations. Promising new approaches to mitigate this problem include the use of a combination of diffusion and generalized eddy-induced advection (Lu et al., 2022; Lu & Kamenkovich, 2025), new eddy-large-scale relations uncovered by machine learning techniques (Zanna & Bolton, 2020), "superparameterization" that models eddy flux divergence directly instead of estimating it from the flux-gradient relation (Berloff & Shevchenko, 2025; Uchida, Deremble, & Popinet, 2022; Uchida, Jamet, et al., 2022), and, even more aggressively, converting the tracer transport model into a purely Lagrangian one that is immune to the numerical blow-off caused by negative diffusivities.

The Eulerian eddy diffusivity estimated using the hybrid approach in the real ocean can be potentially used for global ocean and climate models that do not fully resolve mesoscale eddies. The Lagrangian measurements have been traditionally used to derive a Lagrangian eddy diffusivity that quantifies the rate of particle dispersion (e.g., Rühs et al., 2018; Rypina et al., 2012). Our approach provides a new opportunity to derive the real-ocean Eulerian diffusivity—that is arguably more relevant to the eddy parameterization problems—from these valuable measurements, as global Lagrangian data sets have become available (Elipot et al., 2016, 2024). Overall, this study extends the potential of Lagrangian measurements to provide more insights into eddy mixing processes in the ocean. This potential provides strong motivation for new real-ocean Lagrangian experiments with dense spatial coverage, as the most effective means of studying ocean dynamics and material transport. A potential limitation of the proposed method lies in its reliance on knowledge of Lagrangian velocities, which in this numerical study are known exactly but in the real ocean would need to be estimated from Lagrangian trajectories. The trajectory data typically have relatively low temporal resolution in position, which can introduce bias in the particle velocities. Therefore, the results presented in this study may be regarded as a "best-case" scenario for the performance of our approach, as well as a motivation for continuous monitoring of particle positions. The extent to which the temporal resolution of trajectories influences the accuracy of the hybrid method remains an open question and is left for future investigation.

Finally, we do not presume that either the Eulerian or Lagrangian diffusivity provides the "correct" representation of eddy mixing, but rather propose a method of combining two techniques for local estimates of eddy-induced property fluxes. More generally, diffusion itself may be a fundamentally limited model for describing eddy-induced tracer transport. Determining the most appropriate model for eddy tracer dynamics is beyond the scope of this work, but is an important direction for future research.

Appendix A: Idealized Tracers

This study simulates eight idealized passive tracers in total. They are used to overdetermine the eddy transport tensor (Equation 4). Their concentrations are initialized with different horizontal distributions and are taken constant in the vertical direction (Figure A1):

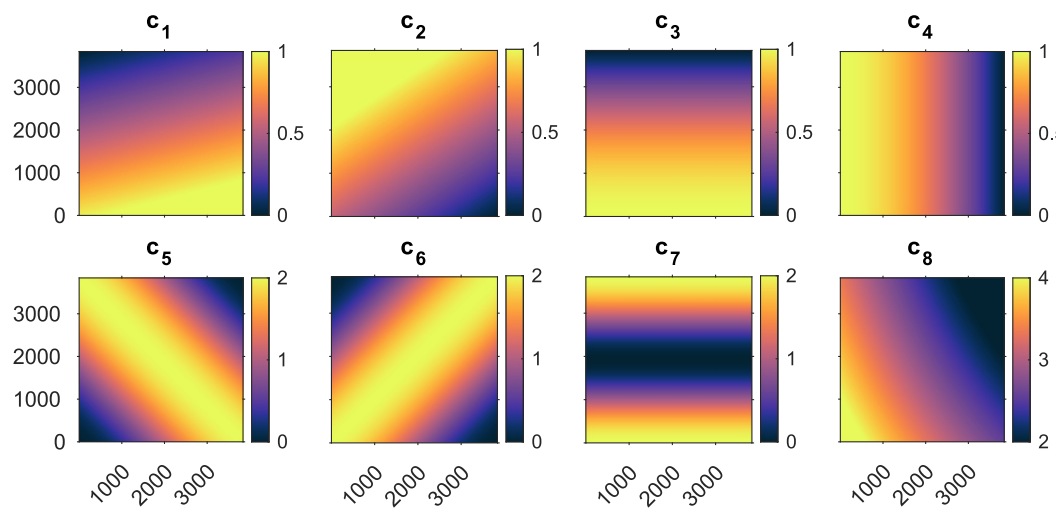

Figure A1. Initial distributions of the idealized tracers.

$$
\begin{aligned}
c_1 &= \frac{1}{\sqrt{17}}\left(\frac{x}{L_x} - 4\frac{y}{L_y} + 4\right), & c_2 &= \frac{1}{\sqrt{13}}\left(-2\frac{x}{L_x} + 3\frac{y}{L_y} + 2\right),\\
c_3 &= \cos\frac{\pi y}{2L_y}, & c_4 &= \cos\frac{\pi x}{2L_x},\\
c_5 &= -\cos\left(\frac{\pi x}{L_x} + \frac{\pi y}{L_y}\right) + 1, & c_6 &= \cos\left(-\frac{\pi x}{L_x} + \frac{\pi y}{L_y}\right) + 1,\\
c_7 &= \cos\frac{2\pi y}{L_y} + 1, & c_8 &= 25 * \left[\frac{\left(0.4\frac{x}{L_x} - 1\right)^2}{9} + \frac{\left(0.4\frac{y}{L_y} - 1\right)^2}{16}\right],
\end{aligned}
\tag{A1}
$$

where L_x and L_y are the domain sizes in the zonal and meridional directions, respectively.

Appendix B: Lagrangian Diffusivity From Single-Particle Statistics

In this section we briefly discuss estimates of the asymptotic (nonlocal) Lagrangian diffusivity tensor from the single-particle dispersion for the ensemble of particles (Griesel et al., 2010; Kamenkovich et al., 2015; Rypina et al., 2012):

$$
\mathbf{K}^L = K^L_{ij}(\mathbf{x}) = \lim_{\tau\to\infty}\frac{1}{2}\frac{\partial D_{ij}(\mathbf{x},\tau)}{\partial t}, \tag{B1}
$$

where D_{ij} is the dispersion matrix:

$$
D_{ij}(\mathbf{x},\tau) = \langle r'_i(\tau|\mathbf{x},t_0) r'_j(\tau|\mathbf{x},t_0)\rangle_l, \tag{B2}
$$

where $\langle\rangle_l$ is an average over the particles, and $r_l(\tau|\mathbf{x},t_0)$ is the displacement of a particle at time τ from its starting position $\mathbf{x}$ and time t_0. The prime denotes that the mean displacement due to the mean flow is subtracted from the total displacement over each time step. This so-called full trajectory-following (FTF) method calculates particle dispersion only due to the eddy flowing but along the particle trajectories in the full (eddy plus mean) flow (Kamenkovich et al., 2015; Rypina et al., 2012). The mean flow is defined by a combination of 120 km × 120 km spatial filter and 2-year time mean, consistent with those when defining the Eulerian diffusivity. Similar to $\mathbf{S}$ (Equation 6), $\mathbf{K}^L$ is also a 2 × 2 symmetric tensor characterizing the (asymptotic) diffusive properties of eddies and can be diagonalized to obtain its major/minor component and diffusion angle. Note that $\mathbf{K}^L$ does not have an advective (anti-symmetric) part by construction unlike the Eulerian eddy transport tensor $\mathbf{K}^E$. The definition of Lagrangian diffusivity (Equation B1) is nonlocal since the time τ needs to be long enough for the dispersion to reach asymptotically the diffusive regime with a linear dispersion growth (i.e., a converging diffusivity). We also attempted to compute the Lagrangian diffusivity from the particle velocity autocorrelation function (Davis, 1991; Zhang & Wolfe, 2024) and found very similar results.

As is described in Section 2.2, we use a group of 1024 particles released from each 120 km × 120 km bin. We track them for each of the six 130-day consecutive intervals (2-year in total) and compute corresponding dispersions D_{ij}. We confirmed that 130 days is sufficient for the growth of dispersion to become linear (linear dispersion growth is observed after about two months in most locations). Then, we calculate the dispersion over the last 40 days in each time interval to get the value of the Lagrangian diffusivity (dispersion rate). The diffusivities for all the six intervals are then finally averaged to give a single $\mathbf{K}^L$ that is representative of the Lagrangian diffusivity for the 2-year period.

Figure B1 shows the components of $\mathbf{K}^L$, which are noticeably different from their Eulerian counterpart (Figures 5a–5c). The major component has a much broader spatial structure and smaller peak values in the jet region, compare to the Eulerian one. This is because the Lagrangian method is fundamentally non-local leading to large biases in the vicinity of the front. The minor component λ_2 is positive in the jet region unlike the Eulerian counterpart. The diffusion angle is nearly purely zonal around the jet, which is due to the shear dispersion caused

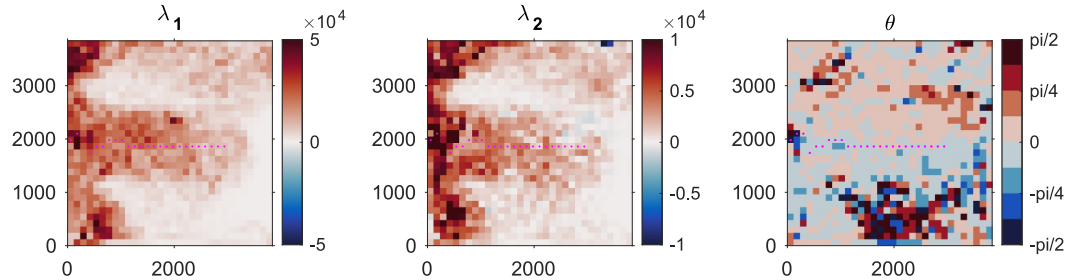

Figure B1. Major, minor components, and the diffusion angle of the Lagrangian eddy diffusivity $\mathbf{K}^L$.

by the main strong flow. These results illustrate fundamental differences between diffusivities estimated by asymptotic Lagrangian and local Eulerian approaches. While each method has its limitations, both offer significant value in specific applications.

Conflict of Interest

The authors declare no conflicts of interest relevant to this study.

Availability Statement

The source code of the MOM6 ocean model configured for this study is available at Lu (2024). The analysis codes are available at Lu (2025a). The data for the Lagrangian trajectories and diffusivity estimates can be found at Lu (2025b).

Acknowledgments
YL and IK acknowledge the support of the NSF Grant 1849990 and the high-performance computing support from Derecho (https://doi.org/10.5065/qx9apg09) provided by NCAR's Computational and Information Systems Laboratory, sponsored by the NSF. We would also like to thank the three anonymous reviewers for their constructive comments that led to improvements to the manuscript.

References

Abernathey, R., Ferreira, D., & Klocker, A. (2013). Diagnostics of isopycnal mixing in a circumpolar channel. *Ocean Modelling*, *72*, 1–16. https://doi.org/10.1016/j.ocemod.2013.07.004

Abernathey, R., Gnanadesikan, A., Pradal, M.-A., & Sundermeyer, M. A. (2022). Isopycnal mixing. In *Ocean Mixing* (pp. 215–256). Elsevier.

Abernathey, R., & Marshall, J. (2013). Global surface eddy diffusivities derived from satellite altimetry. *Journal of Geophysical Research: Oceans*, *118*(2), 901–916. https://doi.org/10.1002/jgrc.20066

Adcroft, A. E. A., Anderson, W., Balaji, V., Blanton, C., Bushuk, M., Dufour, C. O., et al. (2019). The GFDL Global Ocean and Sea Ice Model OM4.0: Model description and simulation features. *Journal of Advances in Modeling Earth Systems*, *11*(10), 3167–3211. https://doi.org/10.1029/2019MS001726

Bachman, S., & Fox-Kemper, B. (2013). Eddy parameterization challenge suite I: Eady spindown. *Ocean Modelling*, *64*, 12–28. https://doi.org/10.1016/j.ocemod.2012.12.003

Bachman, S., Fox-Kemper, B., & Bryan, F. (2015). A tracer-based inversion method for diagnosing eddy-induced diffusivity and advection. *Ocean Modelling*, *86*, 1–14. https://doi.org/10.1016/j.ocemod.2014.11.006

Bachman, S., Fox-Kemper, B., & Bryan, F. O. (2020). A diagnosis of anisotropic eddy diffusion from a high-resolution global ocean model. *Journal of Advances in Modeling Earth Systems*, *12*(2), e2019MS001904. https://doi.org/10.1029/2019MS001904

Balwada, D., Xie, J.-H., Marino, R., & Feraco, F. (2022). Direct observational evidence of an oceanic dual kinetic energy cascade and its seasonality. *Science Advances*, *8*(41), eabq2566. https://doi.org/10.1126/sciadv.abq2566

Bennett, A. (2006). *Lagrangian fluid dynamics*. Cambridge University Press.

Berloff, P. (2015). Dynamically consistent parameterization of mesoscale eddies. Part I: Simple model. *Ocean Modelling*, *87*, 1–19. https://doi.org/10.1016/j.ocemod.2014.12.008

Berloff, P., & Shevchenko, I. (2025). Data-driven eddy closure for oceanic eastward jets. *Frontiers in Marine Science*, *12*, 1623219. https://doi.org/10.3389/fmars.2025.1623219

Brolly, M. T. (2023). Inferring ocean transport statistics with probabilistic neural networks. *Journal of Advances in Modeling Earth Systems*, *15*(6), e2023MS003718. https://doi.org/10.1029/2023ms003718

D'Asaro, E. A., Shcherbina, A. Y., Klymak, J. M., Molemaker, J., Novelli, G., Guigand, C. M., et al. (2018). Ocean convergence and the dispersion of flotsam. *Proceedings of the National Academy of Sciences of the United States of America*, *115*(6), 1162–1167. https://doi.org/10.1073/pnas.1718453115

Davis, R. E. (1991). Lagrangian ocean studies. *Annual Review of Fluid Mechanics*, *23*(1), 43–64. https://doi.org/10.1146/annurev.fl.23.010191.000355

Elipot, S., Faigle, E., Arbic, B. K., & Shriver, J. F. (2024). An integrated dataset of near-surface Eulerian fields and Lagrangian trajectories from an ocean model. *Scientific Data*, *11*(1), 943. https://doi.org/10.1038/s41597-024-03813-z

Elipot, S., Lumpkin, R., Perez, R. C., Lilly, J. M., Early, J. J., & Sykulski, A. M. (2016). A global surface drifter data set at hourly resolution. *Journal of Geophysical Research: Oceans*, *121*(5), 2937–2966. https://doi.org/10.1002/2016jc011716

Ferrari, R., & Nikurashin, M. (2010). Suppression of eddy diffusivity across jets in the Southern Ocean. *Journal of Physical Oceanography*, *40*(7), 1501–1519. https://doi.org/10.1175/2010jpo4278.1

Garrett, C. (1983). On the initial streakness of a dispersing tracer in two- and three-dimensional turbulence. *Dynamics of Atmospheres and Oceans*, *7*(4), 265–277. https://doi.org/10.1016/0377-0265(83)90008-8

Gent, P., & McWilliams, J. (1990). Isopycnal mixing in ocean circulation models. *Journal of Physical Oceanography*, *20*(1), 150–155. https://doi.org/10.1175/1520-0485(1990)020⟨0150:IMIOCM⟩2.0.CO;2

Gent, P., Willebrand, J., McDougall, T., & McWilliams, J. (1995). Parameterizing eddy-induced tracer transports in ocean circulation models. *Journal of Physical Oceanography*, *25*(4), 463–474. https://doi.org/10.1175/1520-0485(1995)025⟨0463:PEITTI⟩2.0.CO;2

Gille, S. T., Speer, K., Ledwell, J. R., & Garabato, A. C. N. (2007). Mixing and stirring in the Southern Ocean. *EOS Transactions of the American Geophysical Union*, *88*(39), 382–383. https://doi.org/10.1029/2007eo390002

Griesel, A., Gille, S. T., Sprintall, J., McClean, J. L., LaCasce, J. H., & Maltrud, M. E. (2010). Isopycnal diffusivities in the Antarctic circumpolar current inferred from Lagrangian floats in an eddying model. *Journal of Geophysical Research*, *115*(C6), C06006. https://doi.org/10.1029/2009jc005821

Griesel, A., McClean, J., Gille, S., Sprintall, J., & Eden, C. (2014). Eulerian and Lagrangian isopycnal eddy diffusivities in the Southern Ocean of an eddying model. *Journal of Physical Oceanography*, *44*(2), 644–661. https://doi.org/10.1175/jpo-d-13-039.1

Griffies, S. (1998). The Gent–McWilliams skew flux. *Journal of Physical Oceanography*, *28*(5), 831–841. https://doi.org/10.1175/1520-0485(1998)028⟨0831:TGMSF⟩2.0.CO;2

Haigh, M., & Berloff, P. (2021). On co-existing diffusive and anti-diffusive tracer transport by oceanic mesoscale eddies. *Ocean Modelling*, *168*, 101909. https://doi.org/10.1016/j.ocemod.2021.101909

Haigh, M., Sun, L., McWilliams, J., & Berloff, P. (2021a). On eddy transport in the ocean. Part II: The advection tensor. *Ocean Modelling*, *165*, 101845. https://doi.org/10.1016/j.ocemod.2021.101845

Haigh, M., Sun, L., McWilliams, J., & Berloff, P. (2021b). On eddy transport in the ocean. Part I: The diffusion tensor. *Ocean Modelling*, *164*, 101831. https://doi.org/10.1016/j.ocemod.2021.101831

Haigh, M., Sun, L., Shevchenko, I., & Berloff, P. (2020). Tracer-based estimates of eddy-induced diffusivities. *Deep Sea Res. I: Oceanographic Research Papers*, *160*, 103264. https://doi.org/10.1016/j.dsr.2020.103264

Haine, T., Griffies, S. M., Gebbie, G., & Jiang, W. (2025). A review of green's function methods for tracer timescales and pathways in ocean models. *Journal of Advances in Modeling Earth Systems*, *17*(7), e2024MS004637. https://doi.org/10.1029/2024ms004637

Holzer, M., & Hall, T. M. (2000). Transit-time and tracer-age distributions in geophysical flows. *Journal of the Atmospheric Sciences*, *57*(21), 3539–3558. https://doi.org/10.1175/1520-0469(2000)057<3539:ttatad>2.0.co;2

Jiang, W., & Haine, T. (2025a). Generation and propagation of eastern subpolar North Atlantic salinity anomalies. https://doi.org/10.21203/rs.3.rs-7005007/v1

Jiang, W., & Haine, T. (2025b). Tracer budgets on Lagrangian trajectories. *Journal of Advances in Modeling Earth Systems*, *17*(9), e2024MS004848. https://doi.org/10.1029/2024ms004848

Kamenkovich, I., Berloff, P., Haigh, M., Sun, L., & Lu, Y. (2021). Complexity of mesoscale eddy diffusivity in the ocean. *Geophysical Research Letters*, *48*(5), e2020GL091719. https://doi.org/10.1029/2020gl091719

Kamenkovich, I., & Garraffo, Z. (2022). Importance of mesoscale currents in AMOC pathways and timescales. *Journal of Physical Oceanography*, *52*(8), 1613–1628. https://doi.org/10.1175/JPO-D-21-0244.1

Kamenkovich, I., Rypina, I., & Berloff, P. (2015). Properties and origins of the anisotropic eddy-induced transport in the North Atlantic. *Journal of Physical Oceanography*, *45*(3), 778–791. https://doi.org/10.1175/JPO-D-14-0164.1

LaCasce, J. (2008). Statistics from Lagrangian observations. *Progress in Oceanography*, *77*(1), 1–29. https://doi.org/10.1016/j.pocean.2008.02.002

LaCasce, Ferrari, R., Marshall, J., Tulloch, R., Balwada, D., & Speer, K. (2014). Float-derived isopycnal diffusivities in the dimes experiment. *Journal of Physical Oceanography*, *44*(2), 764–780. https://doi.org/10.1175/jpo-d-13-0175.1

Laurindo, L. C., Mariano, A. J., & Lumpkin, R. (2017). An improved near-surface velocity climatology for the global ocean from drifter observations. *Deep Sea Research Part I: Oceanographic Research Papers*, *124*, 73–92. https://doi.org/10.1016/j.dsr.2017.04.009

Lebedev, K. V., Yoshinari, H., Maximenko, N. A., & Hacker, P. W. (2007). Velocity data assessed from trajectories of Argo floats at parking level and at the sea surface. *IPRC Technical Note*, *4*(2), 1–16.

Ledwell, J. R., Watson, A. J., & Law, C. S. (1998). Mixing of a tracer in the pycnocline. *Journal of Geophysical Research*, *103*(C10), 21499–21529. https://doi.org/10.1029/98jc01738

Liu, T., Qian, Y.-K., Liu, X., Peng, S., & Chen, D. (2024). Irreversible mixing induced by geostrophic turbulence over the global ocean. *Journal of Physical Oceanography*, *54*(3), 911–928. https://doi.org/10.1175/jpo-d-23-0071.1

Lu, Y. (2024). Double gyre configuration, MOM6-dg: v1.0.0 [Software]. *Zenodo*. https://doi.org/10.5281/zenodo.14263240

Lu, Y. (2025a). Analysis code for calculating Eulerian eddy diffusivity from Lagrangian particle trajectories [Software]. *Zenodo*. https://doi.org/10.5281/zenodo.16789517

Lu, Y. (2025b). Dataset for Lagrangian particle trajectories and hybrid Eulerian-Lagrangian estimates of tracers and eddy diffusivity [Dataset]. *Zenodo*. https://doi.org/10.5281/zenodo.16883801

Lu, Y., & Kamenkovich, I. (2025). Mesoscale eddy-induced sharpening of oceanic tracer fronts. *Journal of Advances in Modeling Earth Systems*, *17*(3), e2024MS004693. https://doi.org/10.1029/2024ms004693

Lu, Y., Kamenkovich, I., & Berloff, P. (2022). Properties of the lateral mesoscale eddy-induced transport in a high-resolution ocean model: Beyond the flux–gradient relation. *Journal of Physical Oceanography*, *52*(12), 3273–3295. https://doi.org/10.1175/JPO-D-22-0108.1

Lumpkin, R., Özgökmen, T., & Centurioni, L. (2017). Advances in the application of surface drifters. *Annual Review of Marine Science*, *9*(1), 59–81. https://doi.org/10.1146/annurev-marine-010816-060641

Lumpkin, R., Treguier, A.-M., & Speer, K. (2002). Lagrangian eddy scales in the northern Atlantic Ocean. *Journal of Physical Oceanography*, *32*(9), 2425–2440. https://doi.org/10.1175/1520-0485-32.9.2425

Mana, P., & Zanna, L. (2014). Toward a stochastic parameterization of ocean mesoscale eddies. *Ocean Modelling*, *79*, 1–20. https://doi.org/10.1016/j.ocemod.2014.04.002

Mariano, A. J., Ryan, E. H., Huntley, H. S., Laurindo, L., Coelho, E., Griffa, A., et al. (2016). Statistical properties of the surface velocity field in the northern Gulf of Mexico sampled by GLAD drifters. *Journal of Geophysical Research: Oceans*, *121*(7), 5193–5216. https://doi.org/10.1002/2015jc011569

Marshall, J., Shuckburgh, E., Jones, H., & Hill, C. (2006). Estimates and implications of surface eddy diffusivity in the Southern Ocean derived from tracer transport. *Journal of Physical Oceanography*, *36*(9), 1806–1821. https://doi.org/10.1175/jpo2949.1

Nakamura, N. (1996). Two-dimensional mixing, edge formation, and permeability diagnosed in an area coordinate. *Journal of the Atmospheric Sciences*, *53*(11), 1524–1537. https://doi.org/10.1175/1520-0469(1996)053⟨1524:TDMEFA⟩2.0.CO;2

Osborn, T. R., & Cox, C. S. (1972). Oceanic fine structure. *Geophysical Fluid Dynamics*, *3*(4), 321–345. https://doi.org/10.1080/03091927208236085

Plumb, R., & Mahlman, J. (1987). The zonally averaged transport characteristics of the GFDL general circulation/transport model. *Journal of the Atmospheric Sciences*, *44*(2), 298–327. https://doi.org/10.1175/1520-0469(1987)044<0298:tzatco>2.0.co;2

Poje, A. C., Özgökmen, T. M., Lipphardt, B. L., Haus, B. K., Ryan, E. H., Haza, A. C., et al. (2014). Submesoscale dispersion in the vicinity of the deepwater horizon spill. *Proceedings of the National Academy of Sciences of the United States of America*, *111*(35), 12693–12698. https://doi.org/10.1073/pnas.1402452111

Prandtl, L. (1925). Bericht über untersuchungen zur ausgebildeten turbulenz. *Zeitschrift für Angewandte Mathematik und Mechanik*, *5*(2), 136–139. https://doi.org/10.1002/zamm.19250050212

Prants, S. (2025). Dynamical systems theory approach in oceanography: A review on achievements, limitations, verification and validation of Lagrangian methods. *Frontiers in Marine Science*, *12*, 1621820. https://doi.org/10.3389/fmars.2025.1621820

Qian, Y.-K., Peng, S., & Liang, C.-X. (2019). Reconciling Lagrangian diffusivity and effective diffusivity in contour-based coordinates. *Journal of Physical Oceanography*, *49*(6), 1521–1539. https://doi.org/10.1175/JPO-D-18-0251.1

Qian, Y.-K., Peng, S., Wen, X., & Liu, T. (2022). Quantifying local, instantaneous, irreversible mixing using Lagrangian particles and tracer contours. *Journal of Physical Oceanography*, *52*(4), 741–757. https://doi.org/10.1175/JPO-D-21-0260.1

Rühs, Zhurbas, V., Koszalka, I. M., Durgadoo, J. V., & Biastoch, A. (2018). Eddy diffusivity estimates from Lagrangian trajectories simulated with ocean models and surface drifter data—A case study for the greater Agulhas system. *Journal of Physical Oceanography*, *48*(1), 175–196. https://doi.org/10.1175/jpo-d-17-0048.1

Rypina, I., Pratt, L., & Lozier, S. (2011). Near-surface transport pathways in the North Atlantic Ocean: Looking for throughput from the subtropical to the subpolar gyre. *Journal of Physical Oceanography*, *41*(5), 911–925. https://doi.org/10.1175/2011JPO4498.1

Rypina, Kamenkovich, I., Berloff, P., & Pratt, L. (2012). Eddy-induced particle dispersion in the near-surface North Atlantic. *Journal of Physical Oceanography*, *42*(12), 2206–2228. https://doi.org/10.1175/JPO-D-11-0191.1

Sebille, E. V., Griffies, S. M., Abernathey, R., Adams, T. P., Berloff, P., Biastoch, A., et al. (2018). Lagrangian ocean analysis: Fundamentals and practices. *Ocean Modelling*, *121*, 49–75. https://doi.org/10.1016/j.ocemod.2017.11.008

Sun, L., Haigh, M., Shevchenko, I., Berloff, P., & Kamenkovich, I. (2021). On non-uniqueness of the mesoscale eddy diffusivity. *Journal of Fluid Mechanics*, *920*, A32. https://doi.org/10.1017/jfm.2021.472

Sun, L., Uchida, T., Penduff, T., Dewar, W. K., Deremble, B., Poje, A. C., et al. (2025). On the dynamics of the subtropical mode water from an ensemble view. *Authorea Preprints*. https://doi.org/10.22541/essoar.174802928.80389595/v1

Taylor, G. I. (1921). Diffusion by continuous movements. *Proceedings of the London Mathematical Society*, *s2–20*(1), 196–212. https://doi.org/10.1112/plms/s2-20.1.196

Uchida, T., Balwada, D., Jamet, Q., Dewar, W. K., Deremble, B., Penduff, T., & Le Sommer, J. (2023). Cautionary tales from the mesoscale eddy transport tensor. *Ocean Modelling*, *182*, 102172. https://doi.org/10.1016/j.ocemod.2023.102172

Uchida, T., Deremble, B., & Popinet, S. (2022). Deterministic model of the eddy dynamics for a midlatitude ocean model. *Journal of Physical Oceanography*, *52*(6), 1133–1154. https://doi.org/10.1175/JPO-D-21-0217.1

Uchida, T., Jamet, Q., Dewar, W., Sommer, J. L., Penduff, T., & Balwada, D. (2022). Diagnosing the thickness-weighted averaged eddy-mean flow interaction from an eddying North Atlantic ensemble: The Eliassen-palm flux. *Journal of Advances in Modeling Earth Systems*, *14*(5), e2021MS002866. https://doi.org/10.1029/2021ms002866

Vallis, G. K. (2017). *Atmospheric and oceanic fluid dynamics*. Cambridge University Press.

Wagner, P., Rühs, S., Schwarzkopf, F., Koszalka, I., & Biastoch, A. (2019). Can Lagrangian tracking simulate tracer spreading in a high-resolution ocean general circulation model? *Journal of Physical Oceanography*, *49*(5), 1141–1157. https://doi.org/10.1175/JPO-D-18-0152.1

Young, W. (2012). An exact thickness-weighted average formulation of the Boussinesq equations. *Journal of Physical Oceanography*, *42*(5), 692–707. https://doi.org/10.1175/jpo-d-11-0102.1

Young, W., Rhines, P., & Garrett, C. (1982). Shear-flow dispersion, internal waves and horizontal mixing in the ocean. *Journal of Physical Oceanography*, *12*(6), 515–527. https://doi.org/10.1175/1520-0485(1982)012<0515:sfdiwa>2.0.co;2

Zanna, L., & Bolton, T. (2020). Data-driven equation discovery of ocean mesoscale closures. *Geophysical Research Letters*, *47*(17), e2020GL088376. https://doi.org/10.1029/2020GL088376

Zhang, W., & Wolfe, C. (2022). On the vertical structure of oceanic mesoscale tracer diffusivities. *Journal of Advances in Modeling Earth Systems*, *14*(6), e2021MS002891. https://doi.org/10.1029/2021MS002891

Zhang, W., & Wolfe, C. L. P. (2024). Inferring tracer diffusivity from coherent mesoscale eddies. *Journal of Advances in Modeling Earth Systems*, *16*(4), e2023MS004004. https://doi.org/10.1029/2023MS004004

Zhurbas, V., Lyzhkov, D., & Kuzmina, N. (2014). Drifter-derived estimates of lateral eddy diffusivity in the world ocean with emphasis on the Indian Ocean and problems of parameterisation. *Deep Sea Research Part I: Oceanographic Research Papers*, *83*, 1–11. https://doi.org/10.1016/j.dsr.2013.09.001

Zhurbas, V., & Oh, I. S. (2003). Lateral diffusivity and Lagrangian scales in the Pacific Ocean as derived from drifter data. *Journal of Geophysical Research*, *108*(C5), 3141. https://doi.org/10.1029/2002jc001596

Zhurbas, V., & Oh, I. S. (2004). Drifter-derived maps of lateral diffusivity in the Pacific and Atlantic oceans in relation to surface circulation patterns. *Journal of Geophysical Research*, *109*(C5), C05015. https://doi.org/10.1029/2003jc002241